FIG. 3. Postnatal growth retardation in SERP1$^{-/-}$ mice. A. Survival of neonatal SERP1$^{+/+}$, SERP1$^{+/-}$, and SERP1$^{-/-}$ mice. The number of mice at birth was designated as 100 in each group. SERP1$^{-/-}$ mice in a C57BL/6 background have lower viability than SERP1$^{-/-}$ mice in a 129Sv/J × C57BL/6 background. B. Weight gain in neonatal genetically manipulated SERP1 mice of the indicated genotype. C. Representative photograph of SERP1$^{-/-}$ versus SERP1$^{+/+}$ littermate siblings in the 129Vs/J × C57BL/6 background.

adulthood (Fig. 3A). Body weights of SERP1$^{-/-}$ mice were reduced to 60% ± 12% of those of SERP1$^{+/+}$ mice in the 129Sv/J × C57BL/6 and to 44% ± 13% of those of SERP1$^{+/+}$ mice in the C57BL/6 mice at 4 weeks after birth. If the body weight of a SERP1$^{-/-}$ mouse was less than 40% of that of a SERP1$^{+/+}$ mouse of the same age, or if weight gain stopped for several days, these animals would usually die. Autopsies of nonsurviving SERP1$^{-/-}$ mice revealed amounts of milk in the gut comparable to those of other mice. Blood glucose levels and liver glycogen contents of low-weight SERP$^{-/-}$ animals were not significantly different from those of other genotypes during the period from 1 to 4 weeks of age. These data indicate that the high mortality of SERP$^{-/-}$ mice was not likely due to reduced nursing or impaired intestinal absorption.

Once SERP1$^{-/-}$ mice survived to the age of 4 weeks, their growth and body weight steadily increased. By 12 weeks of age, body weights of SERP1$^{-/-}$ animals recovered to ~75% of those of SERP1$^{+/+}$ mice in both backgrounds (Fig. 3B).

Effects of the SERP1 gene deletion on glucose homeostasis and insulin biosynthesis. High levels of SERP1 expression in pancreas and in MIN6 cells (Fig. 1) led us to investigate the role of SERP1 in glucose homeostasis and insulin biosynthesis/secretion. i.p.-GTT were performed using mice between 10 and 20 weeks of age to minimize the effect of growth retardation in SERP1$^{-/-}$ mice. Both male and female SERP1$^{-/-}$ mice revealed impaired glucose tolerance (Fig. 4AI and AII). Increased blood glucose levels in SERP1$^{-/-}$ mice were most prominent between 30 min and 60 min after glucose infusion. In the later phase (120 min after glucose injection) of i.p.-GTT, glucose levels in SERP1$^{-/-}$ mice were close to that observed in wild-type controls. In contrast, ITT revealed no significant difference in blood glucose levels between SERP1$^{+/+}$ and SERP1$^{-/-}$ mice after insulin administration (data not shown), suggesting that impaired glucose tolerance in SERP1$^{-/-}$ animals was not due to insulin resistance in peripheral tissue. Histological analysis of pancreatic tissue demonstrated islets of comparable size (Fig. 4B) and immunoreactivity with anti-insulin antibody (data not shown) when SERP1$^{-/-}$ mice were compared with wild-type controls.

To further analyze the effect of SERP1 on insulin biosynthesis/secretion, pancreatic islets were isolated from mice and stimulated by exposure to media with high glucose (22 mM; Fig. 4C). There was only a slight difference in insulin secretion at 15 min after stimulation when islets from the different genotypes were compared (SERP1$^{+/+}$, SERP1$^{+/-}$, and SERP1$^{-/-}$). However, by 30 to 60 min, insulin secretion continued to increase in islets from wild-type controls but not in islets from SERP1$^{-/-}$ mice. It was not until the 60- to 120-min time period that insulin secretion in islets from SERP1$^{-/-}$ mice began to increase again. By 120 min, comparable levels of insulin were present in the supernatants of islets from each genotype.

Metabolic labeling of isolated islets followed by immunoprecipitation with anti-insulin antibody was performed to measure proinsulin/insulin biosynthesis/processing directly after glucose stimulation. In islets from SERP1$^{+/+}$ mice, proinsulin biosynthesis started and reached a peak at 30 to 60 min after glucose stimulation (Fig. 4D, lane 2). Thereafter, it gradually decreased (Fig. 4D, lanes 3 and 4). In contrast, islets from SERP1$^{-/-}$ mice showed a delay in proinsulin biosynthesis that

F4

F3   age, SERP1$^{-/-}$ mice displayed increased mortality (Fig. 3A) and growth retardation (Fig. 3B). Approximately 60% and 35% of SERP1$^{-/-}$ mice in a mixed 129Sv/J × C57BL/6 (n = 16) and C57BL/6 (n = 12) background, respectively, grew to
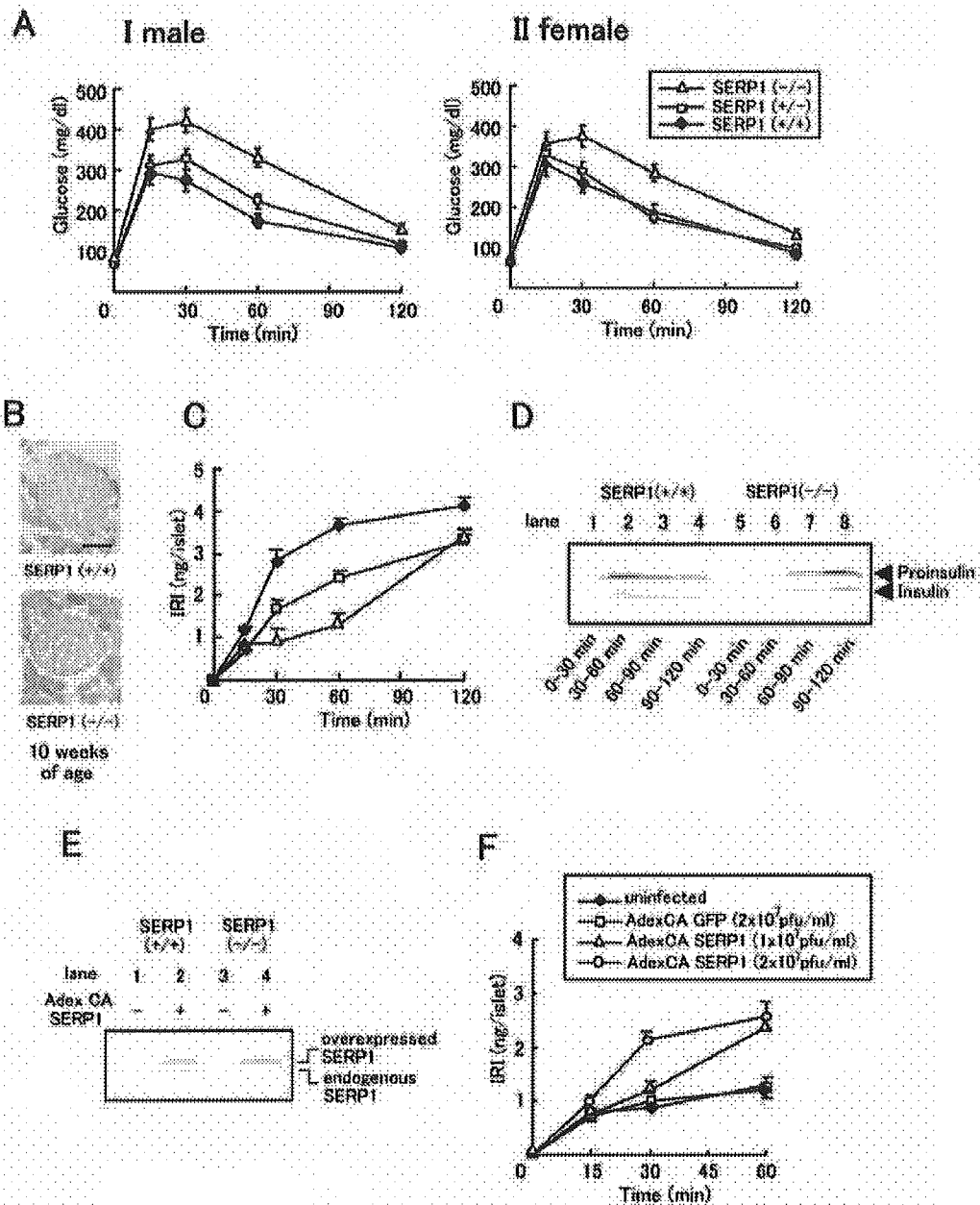
FIG. 4. Impaired glucose tolerance and delayed biosynthesis of insulin in SERP1$^{-/-}$ mice. A. i.p.-GTT were performed on SERP1$^{+/+}$, SERP1$^{+/-}$, and SERP1$^{-/-}$ mice at 10 weeks. Values shown are means ± standard deviations (n = 10 in panel I and n = 6 in panel II). B. Hematoxylin-and-eosin-stained SERP1$^{-/-}$ and SERP1$^{+/+}$ pancreas (10 weeks of age). Bar, 50 μm. C. Insulin release from pancreatic islets isolated from SERP1 mice of the indicated genotype. Islets were incubated in medium containing 22 mM glucose for the indicated times. Insulin levels in the medium were measured by ELISA. Values shown are means ± standard deviations (n = 4). D. Insulin biosynthesis in SERP1$^{+/+}$ (lanes 1 to 4) and SERP1$^{-/-}$ (lanes 5 to 8) islets. Islets were stimulated with high glucose (22 mM) and subjected to metabolic labeling with [^{35}S]Met/Cys for 30 min prior to harvesting. Cell extracts were immunoprecipitated with anti-insulin antibody. E. Adenovirus-mediated transfer of SERP1 cDNA. SERP1$^{+/+}$ and SERP1$^{-/-}$ islets were infected with AdexCA SERP1 (2 × 10^{7} PFU/nl) (lanes 2 and 4) or cultured in the medium alone (lanes 1 and 3), and cell extracts were subjected to Western blotting with anti-SERP1 antibody. F. Rescue experiments with SERP1 cDNA. SERP1$^{-/-}$ islets were infected with AdexCA SERP1 (1 × 10^{7} to 2 × 10^{7} PFU/nl) or AdexCA GFP (2 × 10^{7} PFU/nl) or cultured in medium alone. Insulin release in response to glucose stimulation (22 mM) was monitored by ELISA. Values shown are means ± standard deviations (n = 3).

peaked at 90 to 120 min after glucose stimulation (Fig. 4D, lane 8). The ratio of proinsulin to insulin was not significantly changed in islets from SERP1$^{-/-}$ and wild-type control mice, suggesting that the SERP1 gene deletion affects the biosynthesis of proinsulin but not the conversion of proinsulin to insulin.

To confirm that delayed proinsulin biosynthesis in SERP1$^{-/-}$ islets was due to deletion of the SERP1 gene, rescue experiments were performed using adenovirus-mediated transfer of the SERP1 cDNA as described previously (12). When isolated islets were infected with AdexCA SERP1 (2 × 10^{7} PFU/ml),
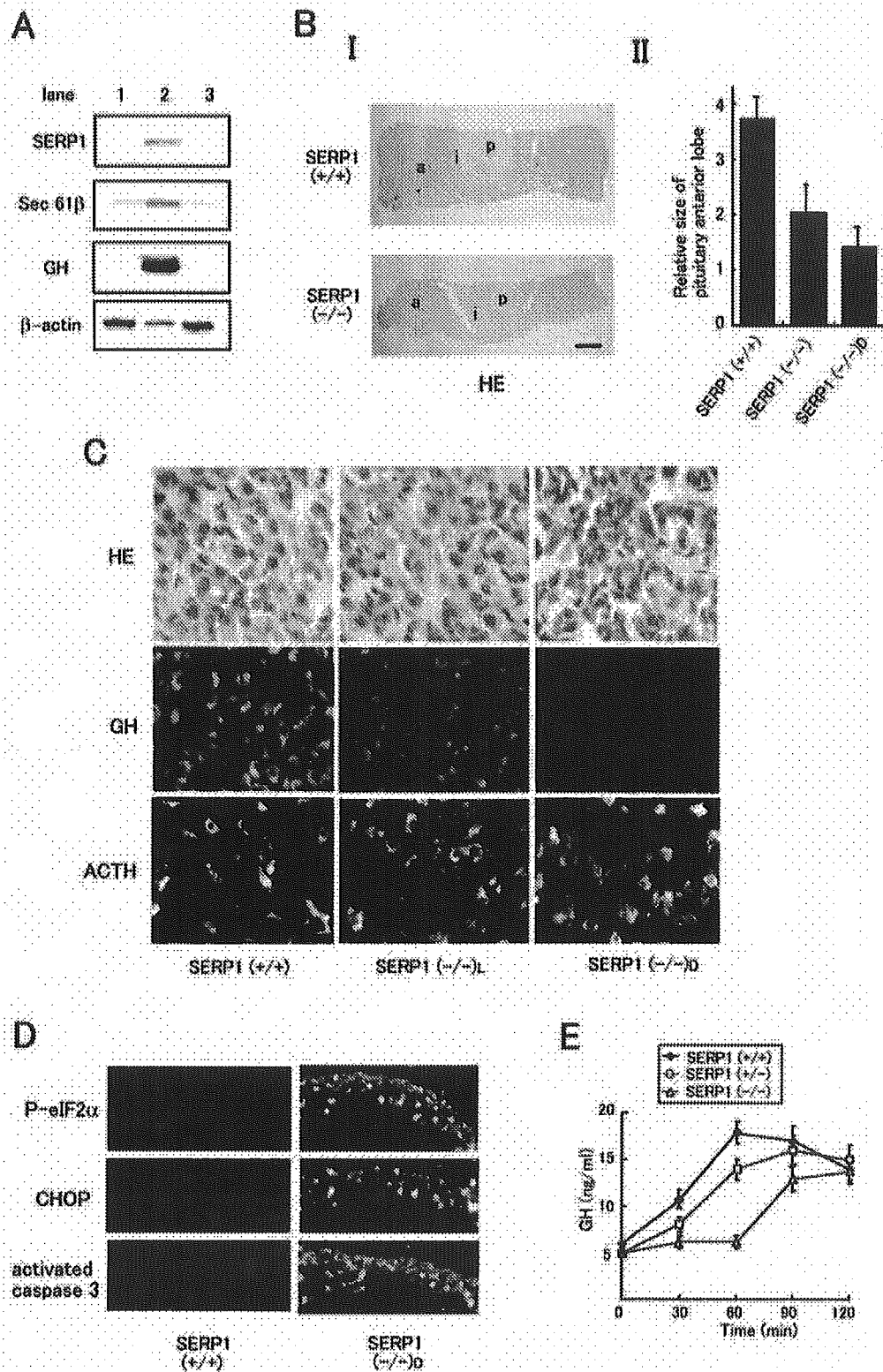
FIG. 5. Reduced size and enhanced ER stress in the SERP1$^{-/-}$ anterior pituitary. A. Expression of SERP1, Sec61β, and GH in the pituitary. Protein extracts (40 µg) from cerebral cortex (lane 1) or pituitary anterior (lane 2) or posterior (lane 3) lobe of C57BL/6 mice (8 weeks) were subjected to Western blotting with indicated antibodies. B. The size of pituitary anterior lobe. I. Pituitary from mice of the indicated genotype (4 to 8 weeks old, coronal section) was stained with hematoxylin and eosin ($n = 4$), and representative micrographs are shown. Bar, 200 µm. II. Relative size of pituitary anterior lobe in SERP1$^{+/+}$, total SERP1$^{-/-}$ (SERP1$^{-/-}$), and dying SERP1$^{-/-}$ (SERP1$^{-/-}$D) mice. Area occupied by the anterior (a) lobe was divided by the combined area of posterior (p) and intermediate (i) (area of the p + i lobes was designated as 1). Values shown are means ± standard deviations ($n = 4$). C. Expressions of GH and ACTH in the anterior pituitary. Pituitary from SERP1$^{+/+}$, living

overexpression of SERP1 antigen was detected by Western blotting as an immunoreactive band just above endogenous SERP1, probably due to the presence of the FLAG epitope (Fig. 4E). In our system, approximately 80% of cells were infected with AdexCA GFP or AdexCA SERP1 at a virus titer of 2×10^7 PFU/ml, based on morphological studies. Adenovirus-infected islets were stimulated in the presence of glucose (22 mM), and insulin secretion was monitored. Insulin secretion was enhanced in a dose-dependent manner in SERP1$^{-/-}$ islets subjected to SERP1 gene transfer 30 to 60 min after glucose challenge (Fig. 4F). Overexpression of GFP, in contrast, was without effect on insulin secretion (Fig. 4F).

Effects of SERP1 gene deletion on the pituitary. Temporal growth retardation in SERP1$^{-/-}$ mice during the postnatal period suggested the possibility that SERP1 might also play an important role in the biosynthesis/secretion of hormones associated with neonatal development. Western blotting of protein extracts from wild-type mouse brain (cerebral cortex) and pituitary anterior and posterior lobes disclosed that both SERP1 and the Sec61 complex (Sec61β) were highly expressed in the anterior pituitary (Fig. 5A). Further analysis using young mice (3 to 8 weeks of age) from each genotype in a 129Sv/J × C57BL/6 background revealed that the anterior pituitary was reduced in size in SERP1$^{-/-}$ mice, compared with wild-type controls, while the intermediate and posterior ones were not affected (Fig.5BI). The area of the anterior lobe (a) is increased 3.6-fold over that of the posterior (p) and intermediate (i) lobes in SERP1$^{+/+}$ mice and increased 2.0-fold in SERP1$^{-/-}$ mice [Fig.5BII, SERP1(+/+) and SERP1(−/−), respectively]. To analyze possible mechanisms underlying the higher mortality in SERP1$^{-/-}$ mice, mutant animals whose body weights were less than 40% of those of SERP1$^{+/+}$ mice were grouped and designated SERP1$^{-/-}$D mice (dying mice). The relative size of the pituitary anterior lobe in SERP1$^{-/-}$D mice was further reduced [Fig.5BII, SERP1(−/−)$_D$; 1.5-fold increase of posterior (p) and intermediate (i) lobes]. Morphological analysis revealed that cells present in the anterior pituitary of living SERP1$^{-/-}$ mice (SERP1$^{-/-}$L) had the same approximate size as those in the other genotypes, while those in the SERP1$^{-/-}$D mice had a smaller size and a smaller area of cytosol (Fig. 5C). Immunohistochemical analysis showed diminished expression of GH, but not of ACTH, in SERP1$^{-/-}$ pituitary (Fig. 5C). Furthermore, expression/activation of molecules associated with ER stress/ER stress-induced cell death was clearly observed in SERP1$^{-/-}$D mice (Fig. 5D).

The overall size/mass of other endocrine tissues or target organs, such as adrenal gland, thyroid, skeletal muscle, and bone, was also relatively reduced in SERP1$^{-/-}$ mice during the neonatal period by up to 60 to 70% compared with SERP1$^{+/+}$ mice. Such widespread changes, however, may be due to nonspecific effects of general growth retardation in SERP1$^{-/-}$ mice.

To analyze the effect of the SERP1 gene deletion on GH biosynthesis and/or secretion, ITT were performed, and blood GH levels were monitored in adult mice (8 weeks old) of each of the genotypes in the 129Sv/J × C57BL/6 background (Fig. 5E). In SERP1$^{+/+}$ mice, blood GH increased in response to hypoglycemia, reaching peak levels by 60 min after insulin infusion (18 ± 2.1 ng/ml). In contrast, there was no increase of GH levels in SERP1$^{-/-}$ mice until the 60-min time point (6 ± 0.5 ng/ml). At 90 min, GH levels in wild-type mice began a gradual decline, while GH levels continued to increase in SERP1$^{-/-}$ mice. After 120 min, each group had similar growth hormone levels (13 to 15 ng/ml).

Effects of the SERP1 gene deletion on the protein translocation and translocation apparatus. To dissect the mechanisms through which SERP1 contributes to rapid biosynthesis of polypeptide hormones in response to stimuli, pancreatic RM were isolated from SERP1$^{+/+}$ and SERP1$^{-/-}$ mice after overnight starvation as described previously (17). Western blot analysis revealed that expression of ER stress-related proteins, such as GRP94, GRP78, or Herp, was enhanced in SERP1$^{-/-}$ RM, compared with wild-type ones (1.5- to 2-fold increase in SERP1$^{-/-}$ RM). Herp is a novel sensitive marker of ER stress that is rapidly degraded at the protein level (7). Phosphorylation of eIF2α, which is responsible for the suppression of protein synthesis in response to ER stress, was also observed to a greater extent in SERP1$^{-/-}$ mice (1.5-fold increase in SERP1$^{-/-}$ RM). In contrast, the amount of membrane-associated ribosomal protein S6 (RPS6) was slightly reduced in SERP1$^{-/-}$ RM (0.7-fold in SERP1$^{-/-}$ RM), and expression of the Sec61 complex (α and β subunits) was similar in both SERP1$^{+/+}$ and SERP1$^{-/-}$ RM (Fig. 6AI and AII). Intracellular insulin/proinsulin levels, determined by ELISA and immunohistochemistry, were not significantly different in the two genotypes (data not shown).

To analyze the effect of SERP1 on protein translocation, an in vitro translation/translocation assay was performed using rabbit reticulocyte lysates. As expected, translation of mRNA of the secretory protein β-lactamase in the absence of canine RM resulted in the synthesis of a precursor containing the signal sequence, while the same reaction performed in the presence of canine RM led to the production of the mature form (Fig. 6B, lanes 1 and 2). Coincubation of β-lactamase mRNA with SERP1$^{+/+}$ or SERP1$^{-/-}$ RM (0.5 to 2 eq) also synthesized processed protein in a dose-dependent manner (Fig. 6B, lanes 3 to 10). However, the yields of both mature and precursor protein were remarkably reduced in the presence of SERP1$^{-/-}$ RM. Coincubation of luciferase (a cytosol protein) mRNA (0.5 to 2 eq) with RM also resulted in reduced protein synthesis (translation) in the presence of SERP1$^{-/-}$ RM (Fig. 6B, lower panel), suggesting that general protein synthesis was inhibited to a greater extent by SERP1$^{-/-}$ RM. A similar trend was obtained when growth hormone (data not shown), prolactin,

SERP1$^{-/-}$ (SERP1$^{-/-}$L), and dying SERP1$^{-/-}$ (SERP1$^{-/-}$D) mice was stained with hematoxylin and eosin (HE) or immunostained with anti-GH and anti-ACTH antibody. D. Expression/activation of molecules associated with ER stress-induced cell death. Pituitary from SERP1$^{+/+}$ or dying SERP1$^{-/-}$ (SERP1$^{-/-}$D) mice was immunostained with the indicated antibodies. E. GH biosynthesis/secretion in SERP1 mice of the indicated genotype (8 weeks of age) after insulin stimulation. ITT were performed as described in Fig. 4, and blood GH levels were measured by ELISA at the indicated times. Values shown are means ± standard deviations ($n = 4$).
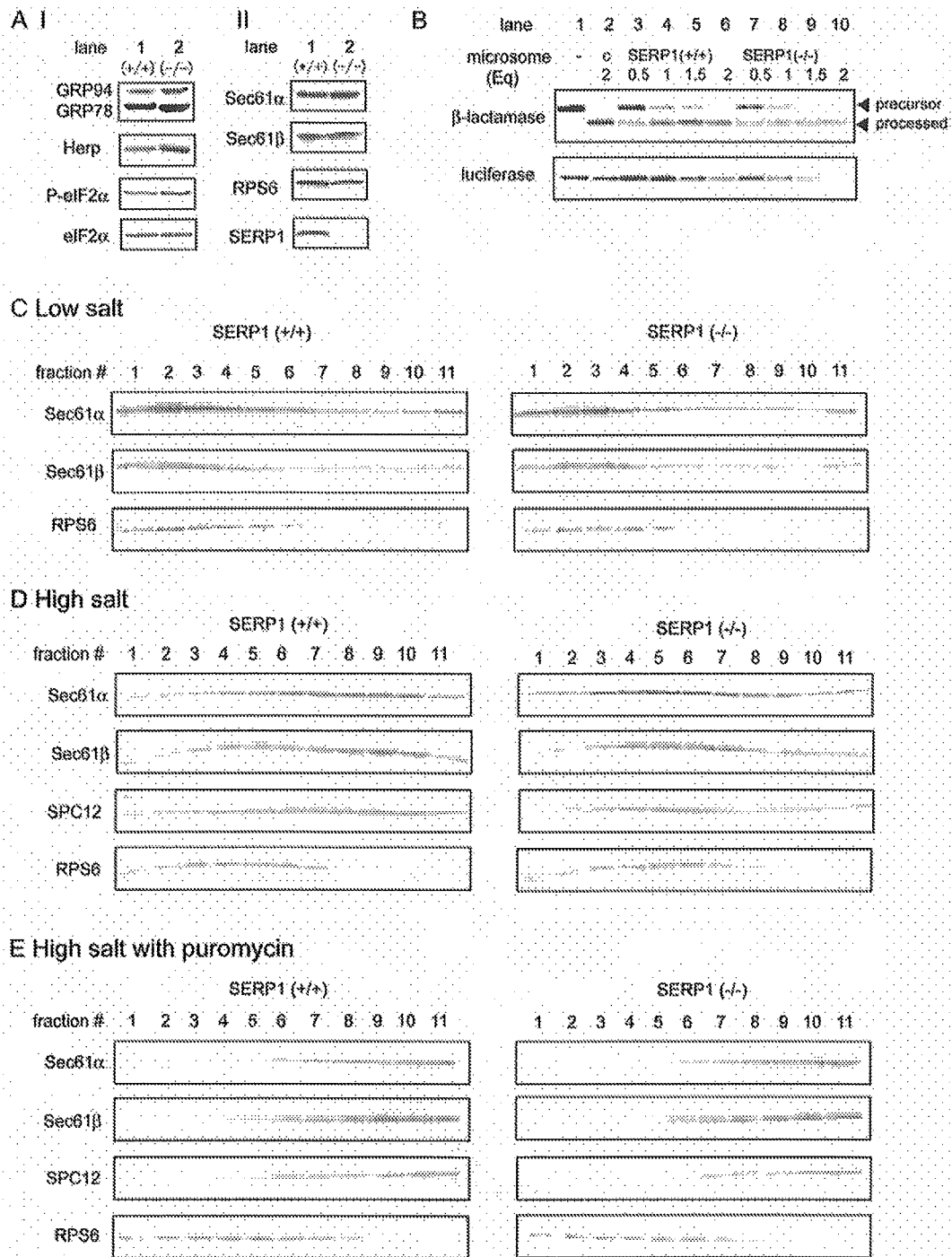
FIG. 6. Characterization of pancreatic RM under basal conditions. A. Expression of ER stress-related molecules and Sec61-associated molecules. RM were isolated from SERP1$^{+/+}$ and SERP1$^{-/-}$ pancreas after 15 h of starvation, as described in the text, and subjected to Western blotting (10 eq/sample) using the indicated antibodies. A typical result of three experiments with independently prepared RM is shown. B. In vitro translation/translocation assay. β-Lactamase (0.1 μg) or luciferase mRNA (0.1 μg) was translated in rabbit reticulocyte lysates in the absence of microsomes (lane 1) or in the presence of canine pancreatic microsomes (2 eq; lane 2), SERP1$^{+/+}$ pancreatic microsomes (0.5 to 2 eq; lanes 3 to 6), or SERP1$^{-/-}$ pancreatic microsomes (0.5 to 2 eq; lanes 7 to 10) for 30 min at 30°C. A typical result of three experiments with independently prepared RM is shown. C to E. Fractionation of RM. RM samples were fractionated using an iodixanol gradient (20 to 30%) in low-salt (C), high-salt (D), and high-salt with puromycin (E) conditions as described in the text and subjected to Western blotting with the indicated antibodies. A typical result of three experiments with independently prepared RM is shown.

or insulin (data not shown) mRNA was used as substrate in ribosome-depleted microsomes (K-RM) from SERP1$^{+/+}$ and SERP1$^{-/-}$ mice.

Fractionation analysis was then performed to compare the status of protein translocation in SERP1$^{+/+}$ and SERP1$^{-/-}$ RM in vivo (2). RM were incubated in low-salt buffer (100 mM KCl) (Fig. 6C), high-salt buffer (600 mM KCl) (Fig. 6D), or high-salt buffer with puromycin (600 mM KCl and 1 mM puromycin) (Fig. 6E) and then fractionated using an iodixanol gradient (20 to 30%). In low-salt conditions, the majority of Sec61 complex cofractionated with the ribosomal protein RPS6, in both SERP1$^{+/+}$ and SERP1$^{-/-}$ RM. However, in high-salt buffer, where translocating polypeptide-free Sec61 was separated from ribosomes, the Sec61 complex and signal peptidase complex 12 (SPC12) cofractionated to a greater extent with RPS6 in SERP1$^{-/-}$ RM, compared with SERP1$^{+/+}$ RM (Fig. 6D). Quantitative studies demonstrated that 50% and 51% of Sec61α and -β, respectively, cofractionated with RPS6 in SERP1$^{+/+}$ RM, while 71% and 69% of Sec61α and -β, respectively, cofractionated with RPS6 in SERP1$^{-/-}$ RM under high-salt conditions (Fig. 7DI and DII; time zero). Addition of puromycin under high-salt conditions separated the Sec61 complex from RPS6 in both genotypes (Fig. 6E), confirming the specific association of Sec61complex with polypeptide-translocating ribosomes in high-salt conditions.

To gain further insight into the mechanism of delayed biosynthesis of insulin/proinsulin in SERP1$^{-/-}$ mice, RM were isolated from both genotypes 45 min and 120 min after glucose stimulation. Western blot analysis revealed that expression of Herp was enhanced at both time points in SERP1$^{-/-}$ RM, compared with SERP1$^{+/+}$ RM, although this increase was less evident 120 min after glucose stimulation (Fig.7AI). In contrast, phosphorylated eIF2α in SERP1$^{-/-}$ RM was enhanced at 45 min after glucose stimulation, though this declined to the baseline levels, comparable to that in SERP1$^{+/+}$ RM, by 120 min (Fig.7AI). Quantitative analysis of phosphorylated eIF2α (P-eIF2α) confirmed enhanced phosphorylation of eIF2α in SERP1$^{-/-}$ RM up to 60 min after glucose stimulation, compared with observations in SERP1$^{+/+}$ RM (Fig.7AII). There was also a slight increase of P-eIF2α immunoreactivity under basal conditions (zero point) in SERP1$^{+/+}$ RM as previously reported (22).

Further fractionation analysis of RM in high-salt conditions revealed that the Sec61 complex cofractionated to a lesser extent with RPS6 in SERP1$^{-/-}$ RM, compared with SERP1$^{+/+}$ RM, at 45 min after glucose exposure (Fig. 7B). In contrast, at 120 min after glucose stimulation, the Sec61 complex again (as in the absence of glucose stimulation [Fig. 6D]) cofractionated to a greater extent with RPS6 in SERP1$^{-/-}$ RM (Fig. 7D). Quantitative analysis showed that, at 45 min, 66% and 68% of Sec61α and -β, respectively, cofractionated with RPS6 in SERP1$^{+/+}$ RM, while 48% and 42% of Sec61α and -β, respectively, cofractionated with RPS6 in SERP1$^{-/-}$ RM (Fig. 7DI and DII; 45 min). At 120 min, in contrast, 63% and 58% of Sec61α and -β, respectively, cofractionated with RPS6 in SERP1$^{+/+}$ RM, while 70% and 71% of Sec61α and -β, respectively, cofractionated in SERP1$^{-/-}$ RM (Fig. 7DI and DII; 120 min).

DISCUSSION

In the current study, we first demonstrated that SERP1, together with the Sec61 complex, was highly expressed in both endocrine and exocrine systems, and its expression was upregulated in response to high glucose. Although deletion of the YSY6 gene, the yeast homolog of SERP1, did not show any apparent phenotype in yeast (unpublished observation), impaired glucose tolerance was observed in SERP1$^{-/-}$ mice at 10 weeks of age. SERP1$^{-/-}$ mice displayed impaired glucose tolerance characterized by a delay in the peak blood glucose levels at 30 min and recovery, with restitution of blood glucose to the range observed in wild-type animals, by 120 min (Fig. 4A). Consistent with these observations, pancreatic islets from SERP1$^{-/-}$ mice displayed a prominent delay of insulin secretion/biosynthesis after glucose challenge (Fig. 4C and D). Although the effect of SERP1 expression was associated with proinsulin biosynthesis which occurs at the ER membrane (Fig. 4D) (8, 19), it is also possible that SERP1 contributes to insulin secretion or energy metabolism in islet cells through the biosynthesis of unknown proteins.

SERP1$^{-/-}$ mice also revealed postnatal growth retardation and increased mortality compared with SERP1$^{+/+}$ littermates. Our search for a cause of growth retardation in SERP1$^{-/-}$ mice led to an investigation of the pituitary. High levels of SERP1 expression were observed in the anterior lobe of the pituitary (Fig. 5A), and its size was significantly smaller in SERP1$^{-/-}$ mice than in wild-type controls (Fig. 5BI and BII). Morphological analysis revealed reduced expression of GH and enhanced ER stress in SERP1$^{-/-}$ mice (Fig. 5C and D). These results suggest that growth arrest and cell death due to enhanced ER stress (1, 13) in the anterior pituitary may be one of the major causes of postnatal growth retardation in SERP1$^{-/-}$ mice. Our preliminary results revealed almost intact morphology and expression of the GH-RH protein in SERP1$^{-/-}$ hypothalamus (data not shown). Analogous to the delayed insulin biosynthesis in response to glucose loads, insulin-stimulated GH production was delayed in adult SERP1$^{-/-}$ mice (Fig. 5E).

Experiments using pancreatic microsomes demonstrated enhanced ER stress (Fig. 6A) and suppression of protein translation (Fig. 6B) in SERP1$^{-/-}$ pancreas, while SERP1 itself did not facilitate translocation of polypeptides in vitro (Fig. 6B; data not shown). Fractionation experiments under basal conditions (i.e., no glucose stimulation) with high salt demonstrated that more Sec61 complexes were tightly associated with ribosomes in SERP1$^{-/-}$ RM than in SERP1$^{+/+}$ RM (Fig. 6D), suggesting that SERP1$^{-/-}$ RM retain more translocating polypeptides at translocation sites. However, intracellular insulin/proinsulin levels (data not shown) or proinsulin biosynthesis in vivo (Fig. 4D, lanes 1 and 5) was not significantly changed in both genotypes, and overall synthesis of β-lactamase (Fig. 6B) or other polypeptide hormones (data not shown) in vitro was suppressed in SERP1$^{-/-}$ RM. Taken together, these observations lead to a hypothesis that SERP1 slightly changes the translocation efficiency in vivo but that its defect is compensated for by an enhanced ER stress response in basal conditions.

Once SERP1$^{+/+}$ and SERP1$^{-/-}$ mice received a glucose challenge, however, the effect of enhanced ER stress in
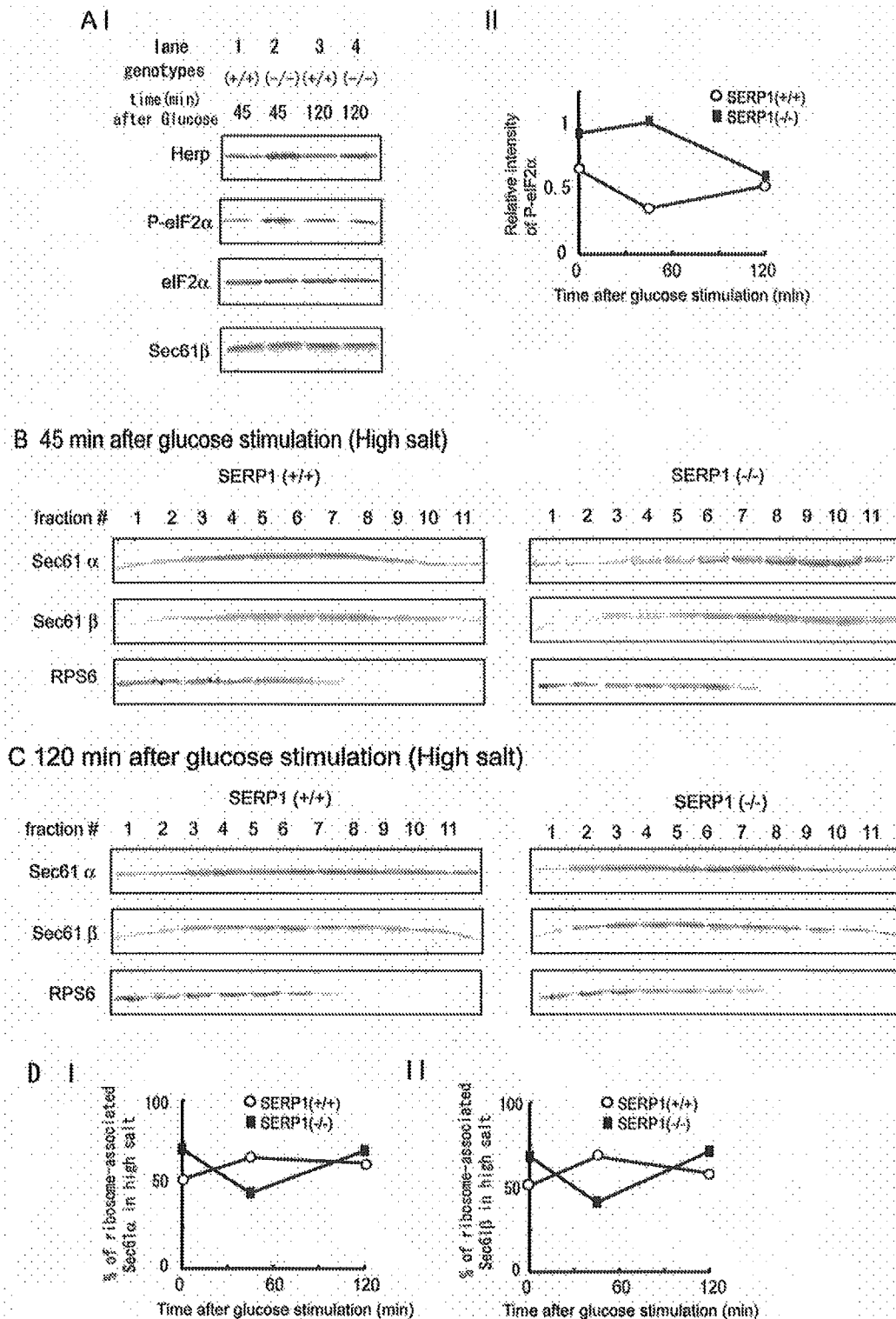
FIG. 7. Characterization of pancreatic RM after glucose stimulation. A. Expression of ER stress-related molecules and the Sec61 complex. I. RM were isolated from SERP1$^{+/+}$ and SERP1$^{-/-}$ pancreas either 45 min or 120 min after glucose injection and subjected to Western blotting (10 eq/sample) using the indicated antibodies. A typical result of three experiments with independently prepared RM is shown. II. Relative intensity of phosphorylated eIF2α antigen after glucose injection. Quantification of P-eIF2α and eIF2α intensities in Fig. 6AI and Fig. 7AI was performed as described in the text, and the relative intensity of P-eIF2α was obtained by dividing the P-eIF2α intensity by eIF2α intensity. B and C. Fractionation of RM. RM samples obtained 45 min (B) and 120 min (C) after glucose injection were fractionated using an iodixanol gradient (20 to 30%) in high-salt conditions and subjected to Western blotting with the indicated antibodies. A typical result of three experiments with independently prepared RM is shown. D. Quantification of Sec61α and -β intensities was performed in Fig. 6D and Fig. 7B and C, and the ratio of ribosome-associated proteins to total proteins is shown.

AQ: J

SERP1$^{-/-}$ mice became more evident. In SERP1$^{+/+}$ mice, levels of phosphorylated eIF2α decreased by 45 min after a glucose load (Fig. 7AI and AII), and at this approximate time, biosynthesis of insulin/proinsulin reached a peak (Fig. 4D, lane 2). Consistent with these data, the Sec61 complex in SERP1$^{+/+}$ mice became more tightly associated with ribosomes (Fig. 7B, DI, and DII), which continued up to 120 min after glucose stimulation. In SERP1$^{-/-}$ mice, however, eIF2α was still phosphorylated, and biosynthesis of insulin/proinsulin was limited to low levels 45 min after glucose load (Fig. 4D, lane 6). More than half of the Sec61 complex in SERP1$^{-/-}$ mice was not tightly associated with ribosome at this time (Fig. 7B, DI, and DII). The status of protein translation in SERP1$^{-/-}$ mice changed 120 min after glucose stimulation. Levels of phosphorylated eIF2α decreased (Fig. 7AI and AII), and biosynthesis of insulin/proinsulin increased (Fig. 4D, lane 8). Furthermore, the Sec61 complex in SERP1$^{-/-}$ mice became more tightly associated with ribosomes again (Fig. 7C, DI, and DII). These observations further support an idea of the close correlation of enhanced ER stress, prolonged suppression of protein translation, and delayed insulin/proinsulin biosynthesis in SERP1$^{-/-}$ RM. Recently, it was reported that p58/IPK, an ER stress-inducible molecule, inhibits phosphorylation of PERK and regulates the PERK-eIF2α pathway (21). In our system, however, expression of p58/IPK decreased 120 min after glucose stimulation (data not shown).

AQ: H

Biosynthesis of polypeptide hormones requires tight regulation to ensure a burst of mature protein production over a short period in response to challenge without induction of protein overload in the ER. In accordance with this concept, the PERK-eIF2α pathway has a critical role in polypeptide hormone biosynthesis. Deletion of the PERK gene or mutational inactivation of eIF2α caused progressive pancreatic cell death and led to severe growth retardation and diabetes mellitus (6, 15, 22). It is noteworthy that phenotypes in SERP1$^{-/-}$ mice were generally milder than were those in PERK$^{-/-}$ or eIF2α-inactivated mice. Although some of the phenotypes in SERP1$^{-/-}$ mice were associated with activation of eIF2α, the PERK-eIF2α pathway may still function as a strong protective tool in SERP1$^{-/-}$ mice. In future studies with SERP1$^{-/-}$ mice, the status of ER stress and protein biosynthesis in different situations where SERP1 is also highly expressed, including exocrine systems and more pathological conditions, should be clarified.

ACKNOWLEDGMENTS

REFERENCES

1. Brewer, J. W., and J. A. Diehl. 2000. PERK mediates cell-cycle exit during the mammalian unfolded protein response. Proc. Natl. Acad. Sci. USA 97:12625–12630.
2. Görlich, D., S. Prehn, E. Hartmann, K.-U. Kalies, and T. A. Rapoport. 1992. A mammalian homolog of SEC61p and SECYp is associated with ribosomes and nascent polypeptides during translocation. Cell 71:489–503.
3. Görlich, D., and T. A. Rapoport. 1993. Protein translocation into proteoliposomes reconstituted from purified components of the endoplasmic reticulum membrane. Cell 75:615–630.
4. Gotoh, M., T. Maki, T. Kiyoizumi, S. Satomi, and A. P. Monaco. 1985. An improved method for isolation of mouse pancreatic islets. Transplantation 40:437–438.
5. Harding, H. P., Y. Zhang, and D. Ron. 1999. Translation and protein folding are coupled by an endoplasmic reticulum resident kinase. Nature 397:271–274.
6. Harding, H. P., H. Zeng, Y. Zhang, R. Jungries, P. Chung, H. Plesken, D. D. Sabatini, and D. Ron. 2001. Diabetes mellitus and exocrine pancreatic dysfunction in perk−/− mice reveals a role for translational control in secretory cell survival. Mol. Cell 7:1153–1163.
7. Hori, O., F. Ichinoda, A. Yamaguchi, T. Tamatani, M. Taniguchi, Y. Koyama, T. Katayama, M. Tohyama, D. M. Stern, K. Ozawa, Y. Kitao, and S. Ogawa. 2004. Role of Herp in the endoplasmic reticulum stress response. Genes Cells 9:457–469.
8. Itoh, N., and H. Okamoto. 1980. Translational control of proinsulin synthesis by glucose. Nature 283:100–102.
9. Kutay, U., E. Hartmann, and T. A. Rapoport. 1993. A class of membrane proteins with a C-terminal anchor. Trends Cell Biol. 3:72–75.
10. Miyazaki, J., K. Araki, E. Yamato, H. Ikegami, T. Asano, Y. Shibasaki, Y. Oka, and K. Yamamura. 1990. Establishment of a pancreatic β cell line that retains glucose inducible insulin secretion: special reference to expression of glucose transporter isoforms. Endocrinology 127:126–132.
11. Mori, K. 2000. Tripartite management of unfolded proteins in the endoplasmic reticulum. Cell 101:451–454.
12. Nagamatsu, S., T. Watanabe, Y. Nakamichi, C. Yamamura, K. Tsuzuki, and S. Matsushima. 1999. α-soluble N-ethylmaleimide-sensitive factor attachment protein is expressed in pancreatic β cells and functions in insulin but not γ-aminobutyric acid secretion. J. Biol. Chem. 274:8053–8060.
13. Oyamadori, S., and M. Mori. 2004. Roles of CHOP/GADD153 in endoplasmic reticulum stress. Cell Death Differ. 11:381–389.
14. Sakaguchi, M., C. Ueguchi, K. Ito, and T. Omura. 1991. Yeast gene which suppresses the defect in protein export of a secY mutant of E. coli. J. Biochem. 109:799–802.
15. Scheuner, D., B. Song, E. McEwen, C. Lie, R. Laybutt, P. Gillespie, T. Saunders, S. Bonner-Weir, and R. Kaufman. 2001. Translational control is required for the unfolded protein response and in vivo glucose homeostasis. Mol. Cell 7:1165–1176.
16. Schröder, K., B. Martoglio, M. Hofmann, C. Holscher, E. Hartmann, S. Prehn, T. A. Rapoport, and B. Dobberstein. 1999. Control of glycosylation of MHC class II-associated invariant chain by translocon-associated RAMP4. EMBO J. 18:4804–4815.
17. Walter, P., and G. Blobel. 1983. Preparation of microsomal membranes for cotranslational protein translocation. Methods Enzymol. 96:84–93.
18. Webb, G. C., M. S. Akbar, C. Zhao, and D. F. Steiner. 2000. Expression profiling of pancreatic β cells: glucose regulation of secretory and metabolic pathway genes. Proc. Natl. Acad. Sci. USA 97:5773–5778.
19. Welsh, M., N. Scherberg, R. Gilmore, and D. F. Steiner. 1986. Translational control of insulin biosynthesis. Evidence for regulation of elongation, initiation and signal-recognition-particle-mediacted translational arrest by glucose. Biochem. J. 235:459–467.
20. Yamaguchi, A., O. Hori, D. M. Stern, E. Hartmann, S. Ogawa, and M. Tohyama. 1999. Stress-associated endoplasmic reticulum protein 1 (SERP1)/ribosome-associated membrane protein 4 (RAMP4) stabilizes membrane proteins during stress and facilitates subsequent glycosylation. J. Cell Biol. 147:1195–1204.
21. Yan, W., C. L. Frank, M. J. Korth, B. L. Sopher, I. Novoa, D. Ron, and M. G. Katze. 2002. Control of PERK eIF2α kinase activity by the endoplasmic reticulum stress-induced molecular chaperone P58^{IPK} Proc. Natl. Acad. Sci. USA 99:15920–15925.
22. Zhang, P., B. McGrath, S. Li, A. Frank, F. Zambito, J. Reinert, M. Gannon, K. Ma, K. McNaughton, and D. R. Cavener. 2002. The PERK eukaryotic initiation factor 2α kinase is required for the development of the skeletal system, postnatal growth, and the function and viability of the pancreas. Mol. Cell. Biol. 22:3864–3874.

Neurobiology

Participation of Autophagy in Storage of Lysosomes in Neurons from Mouse Models of Neuronal Ceroid-Lipofuscinoses (Batten Disease)

Masato Koike,* Masahiro Shibata,*
Satoshi Waguri,* Kentaro Yoshimura,*
Isei Tanida,[†] Eiki Kominami,[†] Takahiro Gotow,[‡]
Christoph Peters,[§] Kurt von Figura,[¶]
Noboru Mizushima,[∥] Paul Saftig,[**] and
Yasuo Uchiyama*

From the Department of Cell Biology and Neurosciences, Osaka
University Graduate School of Medicine, Osaka, Japan; the
Department of Biochemistry,[†] Juntendo University School of
Medicine, Tokyo, Japan; the Laboratory of Cell Biology,[‡] College
of Nutrition, Koshien University, Hyogo, Japan; the Department
of Bioregulation and Metabolism,[∥] Tokyo Metropolitan Institute of
Medical Sciences, Tokyo, Japan; the Institut für Molekuläre
Medizin und Zellforschung,[§] Albert Ludwigs Universität Freibrug,
Freibrug, Germany; the Center for Biochemistry and Molecular
Cell Biology,[¶] Göttingen University, Göttingen, Germany; and the
Department of Biochemistry,[**] University Kiel, Kiel, Germany

In cathepsin D-deficient (CD−/−) and cathepsins B
and L double-deficient (CB−/−CL−/−) mice, abnormal vacuolar structures accumulate in neurons of the
brains. Many of these structures resemble autophagosomes in which part of the cytoplasm is retained but
their precise nature and biogenesis remain unknown.
We show here how autophagy contributes to the accumulation of these vacuolar structures in neurons
deficient in cathepsin D or both cathepsins B and L by
demonstrating an increased conversion of the molecular form of MAP1-LC3 for autophagosome formation
from the cytosolic form (LC3-I) to the membrane-bound form (LC3-II). In both CD−/− and CB−/−
CL−/− mouse brains, the membrane-bound LC3-II
form predominated whereas MAP1-LC3 signals accumulated in granular structures located in neuronal
perikarya and axons of these mutant brains and were
localized to the membranes of autophagosomes, evidenced by immunofluorescence microscopy and
freeze-fracture-replica immunoelectron microscopy.
Moreover, as in CD−/− neurons, autofluorescence
and subunit c of mitochondrial ATP synthase accumulated in CB−/−CL−/− neurons. This suggests that not
only CD−/− but also CB−/−CL−/− mice could be
useful animal models for neuronal ceroid-lipofuscinosis/Batten disease. These data strongly argue for a
major involvement of autophagy in the pathogenesis
of Batten disease/lysosomal storage disorders. (Am J
Pathol 2005, 167:1713–1728)

Autophagy is a highly regulated process involving the
bulk degradation of cytoplasmic macromolecules and
organelles in eukaryotic cells via the lysosomal/vacuolar
system.[1] Although it is induced under starvation, differentiation, and normal growth control,[2] the participation of
autophagy has also been demonstrated in various neurodegenerative disorders.[3] Moreover, it has been shown
that autophagy can trigger a form of cell death distinct
from apoptosis in neurons.[4-6] Thus autophagy appears
to be involved in neurodegenerative disorders.

The most common inherited neurodegenerative disease in childhood is neuronal ceroid-lipofuscinosis (NCL,
or Batten disease), which is categorized as a lysosomal
storage disorder and pathologically characterized by the
accumulation of proteolipids, such as subunit c of mitochondrial ATP synthase and sphingolipid activator proteins in the lysosomes of neurons.[7-10] We have previously
demonstrated that the central nervous system (CNS) neurons in cathepsin D-deficient (CD−/−) mice show a new
form of lysosomal accumulation disease with a phenotype resembling NCLs and subunit c of mitochondrial

ATP synthase accumulates in the lysosomes of the affected neurons.[11,12] Double membrane-bound vacuoles containing part of the cytoplasm are frequently detected in CNS neurons of CD−/− mouse brains near the terminal stage.

It has also been demonstrated that the phenotypes of mice deficient in both cathepsins B and L (CB−/−CL−/− mice) resemble NCLs, but the accumulated substances show no autofluorescence and are immunonegative for subunit c and saposins.[13] However, in neurons of these CD−/− and CB−/−CL−/− mouse brains, the exact nature and biogenesis of the accumulated lysosomal structures remain unknown.

It has recently been found that LC3, light chain 3 of neuronal microtubule-associated protein 1A/B, is a mammalian homolog of yeast Atg8p that is required for autophagosome formation.[14] Immediately after the synthesis of LC3, the protein is converted to the cytoplasmic form, LC3-I, by cleavage at the C-terminal region,[14] which is further converted into a membrane-bound form, LC3-II, by Atg7p and Atg3p, respectively, when autophagy is induced.[15–17] Moreover, LC3-II is localized mainly in the membranes of autophagosomes and, to a lesser extent, within autophagolysosomes.[14] We therefore investigated whether autophagy participates in the accumulation of lysosomal structures in the brain and peripheral tissues of mice deficient in cathepsin D and those doubly deficient in cathepsins B and L by characterizing molecular forms of LC3. Our data showing that the conversion of LC3-I to LC3-II in CD−/− and CB−/−CL−/− mouse brains coincides with the accumulation of lysosomal structures or LC3-positive granules in the neurons, suggest that autophagy is involved in the abnormal storage accumulation in CNS neurons of NCL/lysosomal storage disorders.

Materials and Methods

Animals

The experiments described here were performed in compliance with the regulations of Osaka University Medical School Guideline for the Care and Use of Laboratory Animals. For cathepsin D-, B-, or L-deficient mice,[18–20] heterozygous (+/−) mice were transferred to the Institute of Experimental Animal Sciences, Osaka University Graduate School of Medicine, and kept in conventional or specific pathogen-free facilities on a 12-hour light/dark cycle. To obtain homozygous mice (CD−/−, CB−/−, and CL−/−) mice, heterozygous mice (CD+/−, CB+/−, and CL+/−, respectively) were intercrossed. Selection of homozygous mice from littermates obtained by heterozygous coupling was performed by genomic polymerase chain reaction (PCR) as described previously.[21,22] Briefly, for the selection of CD−/− mice, the template genomic DNA isolated from tail biopsies was examined by CD-exon 4-specific PCR with primers having the following sequences: MCD14 (5′-AGACTAACAGGCCTGT-TCCC-3′) and MCD15 (5′-TCAGCTGTAGTTGCTCA-CATG-3′). The selection of CB−/− mice from littermates obtained by heterozygous coupling was performed by

examining the template genomic DNA isolated from tail biopsies, using CB-exon 4-specific PCR with primers of MCB11 (5′-GGTTGCGTTCGGTGAGG-3′) and MCBGT (5′-AACAAGAGCCGCAGGAGC-3′). The selection of CL−/− mice from littermates obtained by heterozygous coupling was performed by the triple PCR method; the template genomic DNA isolated from tail biopsies was examined using primers of MCL5 (5′-GGAGGAGAGC-GATATGGG-3′), MCL9 (5′-AGCCATTCACCACCTGC-C-3′), and neo756-777 (5′-CGCAGAACCTGCGTGCA-ATCC-3′).

For the generation of CB and CL double-knockout (CB−/−CL−/−) mice, CB−/− mice were bred to CL−/− mice to create progeny that were heterozygous for both cathepsins B and L deletions (CB+/−CL+/− mice). These double heterozygotes were intercrossed to produce mice doubly deficient in both cathepsins B and L (CB−/−CL−/− mice). Most died at approximately P14, as previously reported.[13] The heterozygous mice (CD+/− and CB+/−CL+/− mice) were used as control animals in the present study and showed no pathological phenotypes when examined by histological, immunocytochemical, and biochemical methods.

For the generation of CD−/− mice expressing GFP-LC3 (GFP-LC3/CD−/− mice), six GFP-LC3 transgenic mice (line no. 53)[23] were obtained from Riken BioResource Center (Tsukaba, Japan), crossed with C57BL/6 mice, and maintained as heterozygotes for the GFP-LC3 transgene in the Institute of Experimental Animal Sciences. As mentioned above, the incorporation of the transgene was confirmed by PCR using primers GFP1 (5′-TCCTGCTGGAGTTCGTGACCG-3′) and LC3* (5′-TT-GCGAATTCTCAGCCGTCTTCATCTCTCTCGC-3′). Another primer set mLC3ex3GT (5′-TGAGCGAGCTCAT-CAAGATAATCAGGT-3′) and mLC3ex4AG (5′-GTTA-GCATTGAGCTGCAAGCGCCGTCT-3′) amplifying the third intron of the LC3 genome as an internal control was used. The positive mice were also crossed with CD+/− mice and CD+/− mice heterozygous for the GFP-LC3 transgene (GFP-LC3/CD+/− mice) were generated. GFP-LC3/CD+/− mice were further crossed with CD+/− mice and CD−/− mice heterozygous for the GFP-LC3 transgene (GFP-LC3/CD−/− mice) were obtained.

Antisera

Rabbit antibodies against rat LC3 and rat subunit c of mitochondrial F1F0ATPase were produced and purified by affinity chromatography, as reported previously.[8,24] Monoclonal antibodies against mouse lamp1 (the Developmental Studies Hybridoma Bank, Iowa City, IA) and mouse microglial cells (F4/80) (Serotec, Oxford, UK), respectively, and rabbit polyclonal antibodies against GFP (Abcam, Cambridge, UK) were commercially obtained.

Sampling

CD−/− and CD+/− littermates obtained at postnatal day 8 (P8) to P24 (n = 3 for each stage and each genotype),

CB$-$/$-$CL$-$/$-$ and their littermates at P13 (n = 3 each), and GFP-LC3/CD+/+ and GFP-LC3/CD$-$/$-$ mice at P20 (n = 3 each) were deeply anesthetized with pentobarbital (25 mg/kg i.p.) and fixed by cardiac perfusion with 4% paraformaldehyde buffered with 0.1 mol/L phosphate buffer (pH 7.2), containing 4% sucrose for immunohisto-chemistry, detection of autofluorescence, and periodic acid-Schiff staining, with 1% paraformaldehyde buffered with 0.1 mol/L phosphate buffer (pH 7.2), containing 4% sucrose for freeze-fracture replica immunogold label-ing,[25] and with 2% paraformaldehyde-2% glutaraldehyde buffered with 0.1 mol/L phosphate buffer for ordinary electron microscopy.[11] Immediately after perfusion fixa-tion, brains and peripheral tissues were excised from the mice and processed for immunohistochemistry/cyto-chemistry and ordinary electron microscopy.[11,26]

For light and electron microscopy, brain tissues were quickly removed from the mice and further immersed in the same fixatives for 2 hours. Samples processed for paraffin embedding were cut at 5 μm with a microtome, and those for cryosections were cut at 10 μm with a cryostat (CM3050; Leika, Nussloch, Germany). These sections were placed on silane-coated glass slides and stored at $-$80°C until used. Samples for electron micros-copy were postfixed with 2% OsO_4, dehydrated with a graded series of alcohol, and embedded in Epon 812. Ultrathin sections were cut with an ultramicrotome (Ul-tracut N; Reichert-Nissei, Toyko, Japan), stained with uranyl acetate and lead citrate, and observed with a Hitachi H7100 electron microscope (Hitachi, Tokyo, Ja-pan). For freeze-fracture replica immunogold labeling, the brain tissue was quickly excised from the mice, while cerebral cortical and cerebellar regions were separated from each brain and cut at 100 μm with a vibratome (VT1000S; Leica) at 4°C. Tissue slices were infiltrated with 30% glycerol buffered with 0.1 mol/L phosphate buffer (pH 7.2) until used.

Morphometry

Morphometric analyses were performed according to the method of Uchiyama and Watanabe.[27] In samples ob-tained from CD$-$/$-$ and CD+/$-$ littermates (n = 4 each) at P8, P15, and P23 and CB$-$/$-$CL$-$/$-$ and CB+/$-$CL+/$-$ littermates (n = 4 each) at P13, electron micro-graphs (40 per sample) of the cerebral cortex (layer 5) were taken with systematic random sampling at each corner of 100-mesh grids with a primary magnification of ×7000. Three to five Epon blocks from each mouse were used. After printing at 2.6× the original magnification on projection papers, we estimated the cytoplasmic (perikaryal) volume fraction of lysosomal structures in-cluding various types of autophagic vacuoles (AVs), dense bodies, granular osmiophilic deposit (GROD)-like inclusions, and fingerprint profiles by point counting, us-ing a double-lattice test system of 1.5-cm spacing. AVs were classified as early AVs (AVi), which contain the morphologically intact cytoplasm (see Figure 2A), and late AVs (AVd), which contain partially degraded but identifiable cytoplasmic materials (see Figure 2B).[28–30] In

CD$-$/$-$ and CB$-$/$-$CL$-$/$-$ brains, inclusions that, by electron microscopy, were dense granular and amor-phous in neurons were quite similar to the so-called GRODs, a typical hallmark in infantile NCL;[31] these gran-ules were defined as GROD-like inclusions. In CD$-$/$-$ neurons, distinct points falling on GROD-like inclusions or those surrounded by double-layered membranes resem-bling AVi were counted (see Figure 2D). Moreover, the multilayered lamellar structures that were counted as AVi always contained morphologically intact cytoplasm, and were different from fingerprint profiles that did not contain part of the cytoplasm and possessed tightly and concen-trically arrayed membranes as in the structures observed in juvenile NCL.[31] The volume density (Vv) of each lyso-somal structure was expressed as the percent volume: Vv = (Pi/Pt) × 100 (%), where Pi is the number of points falling on each lysosomal structure and Pt is the number of points falling on the perikarya of large pyramidal neu-rons located in the layer V of the cerebral cortex.

Immunohistochemical Analyses for Light Microscopy

For the detection of LC3 and subunit c, deparaffinized or frozen sections were used and immunostained according to the method described previously.[32] The samples were incubated at 4°C with anti-LC3 (20 μg/ml), anti-subunit c (5 μg/ml), or anti-GFP (4 μg/ml) for 1 to 3 days and further processed for visualization. For double-immunofluores-cent staining, deparaffinized or frozen sections of brain tissues from CD$-$/$-$ and CB$-$/$-$CL$-$/$-$ mice and those from GFP-LC3/CD+/+ and GFP-LC3/CD$-$/$-$ mice were incubated with anti-LC3 and monoclonal anti-lamp1 or F4/80 for 24 hours at 4°C and further with goat anti-rabbit IgG coupled with Alexa 594 (Molecular Probes, Eugene, OR) and goat anti-rat IgG coupled with fluorescein iso-thiocyanate (Cappel, Durham, NC), or coupled with Alexa 594 for 1 hour at room temperature. The stained tissues were viewed with a confocal laser-scanning microscope (LSM510; Carl Zeiss, Jena, Germany).

Freeze-Fracture Replica Immunogold Labeling

To determine the subcellular localization of LC3, the so-dium dodecyl sulfate (SDS)-digested freeze-fracture rep-lica labeling (FRL) technique[33] was applied to chemically fixed brain tissues.[25] Samples were mounted between two gold specimen disks in a specimen-mounting me-dium, polyvinyl alcohol. The disks were quickly frozen in Freon 22 cooled to its freezing point, mounted in a Balzers complementary freeze-fracture apparatus (BAF 400D; Balzers, Furstentum, Lichtenstein) and immedi-ately shadowed unidirectionally by evaporating platinum-carbon at 45° to the vertical carbon support. The thick-ness of platinum (2.5 nm) was controlled with a quartz crystal monitor. To release the replicas from the speci-men carrier, the carrier was immersed gently in phos-phate-buffered saline (PBS). After floating off, the pieces of the replicas were transferred to a detergent solution (2.5% SDS, 10 mmol/L Tris-HCl, pH 9). SDS digestion

was performed for 24 hours at room temperature with vigorous constant stirring. The replicas were moved to the same detergent solution, washed for at least one additional 1 hour, rinsed four times in PBS (5 minutes each), and placed on drops of 1 to 10% bovine serum albumin (BSA) in PBS (BSA-PBS) for 30 minutes at room temperature. For immunostaining, rabbit polyclonal anti-LC3 antibody and 10-nm colloidal gold conjugated goat anti-rabbit IgG were used. The replicas, picked up on grids, were observed with a Hitachi H7100 electron microscope.

Immunoblot Analysis

Anesthetized mice were killed by decapitation and each excised tissue was independently homogenized in 2 ml of 0.05 mol/L Tris-buffered 0.15 mol/L saline containing 1% Triton X-100 and a protease inhibitor cocktail (Boehringer Mannheim, Mannheim, Germany) by a Polytron homogenizer (Kinematica, Littau, Switzerland) at 80% maximal speed. After centrifuging twice at 10,500 × g for 10 minutes at 4°C, the protein concentration in the supernatants were determined using the BCA protein assay system (Pierce, Rockford, IL). The samples were analyzed by immunoblotting according to the method of Towbin and colleagues.[34] After immunostaining with anti-LC3 (1 μm/ml) or polyclonal anti-GFP (0.4 μm/ml), immunodetection was performed with a chemiluminescent ECL kit (Amersham, Arlington Heights, IL). The density of each protein band in the blotting was measured using a densitometer (Molecular Dynamics, Sunnyvale, CA) and the ratio of LC3-I to LC3-II molecules was calculated for brain tissues. In the case of peripheral tissues, the density of LC3-II was measured and presented as a mean ± SD from three independent experiments.

Reverse Transcriptase (RT)-PCR Analysis

RT-PCR analysis of LC3 was performed according to the method described previously.[35] Total RNAs were extracted from neuronal tissues of CD +/− and −/− mice at P8, P15, and P22 and CB+/−CL+/− and CB−/−CL−/− mice at P13, using a Polytron homogenizer for 1 minute in Isogen (Nippon Gene, Tokyo, Japan). To avoid contamination with genomic DNA, 40 to 50 μg of total RNAs were treated with 0.2 U/ml DNase I (Nippon Gene) for 20 minutes at 37°C. Then, 2.0 μg/ml of the total RNAs were used for cDNA synthesis using AMV reverse transcriptase (Takara, Tokyo, Japan) and amplification of the LC-3 and β-actin cDNAs were performed by PCR using EX taq HS (Takara). The PCR amplification was performed at 95°C for 5 minutes, followed by 30 cycles of 95°C for 30 seconds, 55°C (for LC-3) or 60°C (for β-actin) for 30 minutes, and 72°C for 30 minutes using the primer sets for LC-3 (GenBank accession number NM_026160) (forward: 5'-GTGGGCCGCTCTAGGCACCAA-3', reverse: 5'-CTCTTTGATGTCACGCACGATTTC-3'; 540 bp) and β-actin (GenBank accession number M12481) (forward: 5'-GTGGGCCGCTCTAGGCACCAA-3', reverse: 5'-CTC-TTTGATGTCACGCACGATTTC-3'; 540 bp).
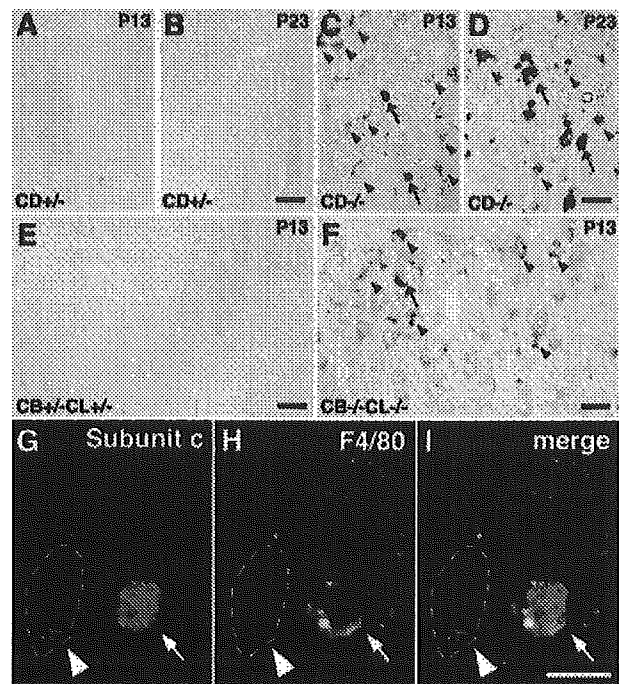

Figure 1. Immunostaining for subunit c of mitochondrial ATP synthase in the cerebral cortex obtained from CD+/− (A, C) and CD−/− (B, D) mice at P13 (A, B) and P23 (C, D) and from CB+/−CL+/− (E) and CB−/−CL−/− (F) mice at P13. A–D: Positive staining for subunit c is intense in neurons (arrowheads) and microglial cells (arrows) of the CD−/− mouse brain (B, D), but not in those of the control littermate brain (A, C). The immunoreactivity is weaker in neurons of CD−/− at P13 (C, arrowheads). E and F: Similar localization patterns of subunit c to those in A to D are observed in the cerebral cortex of CB+/−CL+/− (E) and CB−/−CL−/− (F) mice, although the immunoreactivity is weak in neurons (arrowheads). G–I: Double immunostaining of subunit c and F4/80 in the cerebral cortex of a CB−/−CL−/− mouse at P13. Positive signals for subunit c (red) are large and intense and co-localized in a F4/80-positive microglial cell (arrows), whereas they are fine granular and localized in a F4/80-negative neuron that is marked by arrowheads. Scale bars, 20 μm.

Results

Accumulation of Autophagosome-Like Inclusion Bodies in Both CD−/− and CB−/−CL−/− Mouse Neuronal Perikarya

As described previously,[11] massive autofluorescent granules, which are immunopositive for subunit c of mitochondrial ATP synthase and lysosomal cathepsin B, had accumulated in the neuronal cell perikarya of CD−/− mouse brains near the terminal stage (data not shown). Indeed, immunoreactivity for subunit c was intensely detected in neurons and microglial cells of CD−/− mouse brains at P13 and P23, but not in those in the control littermate mice (Figure 1, A–D).

It has been shown that the phenotype of CB−/−CL−/− is highly reminiscent of NCLs, both of which demonstrate the early and severe brain atrophy; however, the former does not show immunoreactivity for subunit c in brain tissue and ultrastructural characteristics of accumulated lysosomal compartments in CB−/−CL−/− neurons are different from those in NCLs.[13] The present study also generated CB−/−CL−/− mice by crossing CB+/−CL+/− mice and examined morphological and

biochemical characteristics of these mutant mice. In CB−/−CL−/− mice at P13, localization patterns of subunit c in brain tissue were very similar to those in CD−/− mice at the same postnatal age, although the immunoreactivity for subunit c in these two models at P13 was much weaker than in CD−/− brains at P23. The immunoreactivity was more intense in microglial cells than in neurons in CD−/− and CB−/−CL−/− brains at any stages examined (Figure 1, C, D, and F). The positive signal for subunit c was not detected in the control littermate brains (Figure 1, A, B, and E). To confirm the presence of the subunit c immunoreactivity in neurons and microglial cells, double immunostaining of subunit c and F4/80 was performed in the cerebral cortex of CB−/−CL−/− mice at P13; intense staining for subunit c was clearly visible in F4/80-immunopositive microglial cells, while granular fluorescence for subunit c was also detected in F4/80-negative neurons (Figure 1, G–I). Moreover, autofluorescence was discerned in neurons and microglial cells in CB−/−CL−/− mouse brains at P13, while these mutant neurons were intensely positive for periodic acid-Schiff staining (Supplemental Figure 1 at http://ajp.amjpathol.org).

Electron microscopic observations in neurons of CD−/− mouse brain tissues showed that these lysosomal structures that have been shown to possess subunit c[11] coincided with granular inclusions and autophagosome/autophagolysosome-like structures (Figure 2A; Figure 3, A, B, D, and E), the former of which have strong similarity to GRODs, a typical hallmark of NCLs.[31] Autophagosome-like structures containing morphologically intact cytoplasm are often surrounded with multilayered lamellar structures (Figure 2A; Figure 3, A and D). Moreover, these multilayered lamellar structures were different from fingerprint-like structures that did not contain part of the cytoplasm and had tightly and concentrically arrayed membranes and strongly resembled fingerprint profiles, a typical hallmark of NCLs.[31] In CB−/−CL−/− mouse brains, multilayered lamellar structures appeared only occasionally, while fingerprint profiles were totally absent (Table 1).

In semithin sections of CB−/−CL−/− mouse brains, numerous granules that were stained by toluidine blue accumulated in neuronal cell perikarya, dendrites, and axons (data not shown), as has been shown in CD−/− mouse brains.[11] By electron microscopy, most of the lysosome-like structures in the neurons of CB−/−CL−/− mouse brains resembled GRODs (GROD-like inclusions) and autophagosomal (autophagosome-like) structures (Figure 2, B and C). In the corpus callosum of the mouse brains, autophagosome-like structures abundantly accumulated in unmyelinated and myelinated nerve fibers (Figure 2, D and E), while microglia-like cells were often observed to possess heterophagosomes containing numerous autophagosome-like structures (Figure 2D, inset). Most vacuolar structures in the axons were encircled by double-membrane saccules (Figure 2E). In dendrites of cerebral cortical neurons and Purkinje neurons of CD−/− and CB−/−CL−/− mice, granular structures also accumulated, but these accumulated structures were similar to those observed in the neuronal perikarya

(Supplemental Figure 2A at http://ajp.amjpathol.org). Like axons in the corpus callosum, autophagosome-like structures that were encircled by double-membrane saccules accumulated in axons of the cerebellum in CB−/−CL−/− mice (Supplemental Figure 2B at http://ajp.amjpathol.org).

It has been shown that autophagosomes undergo stepwise maturation by fusing with endosomes and/or lysosomes,[36] while two types of AVs in this maturation process are distinguishable by electron microscopy;[28,30] nascent or immature AVs encircled by endoplasmic reticulum (ER)-like membrane saccules contain part of the morphologically intact cytoplasm (AVi) (Figure 3, A and D) and mature AVs encircled by a single membrane possess degraded but morphologically identifiable cytoplasmic materials and structures (AVd) (Figure 3B). It is interesting that lysosome-like structures such as dense bodies, GROD-like inclusions, and autophagosome-like structures themselves were often surrounded, along with part of the cytoplasm, by membrane saccules (Figure 2, A–C; Figure 3, A–D), indicating that autophagosome formation is abundant. In addition to GROD-like inclusions and AVs, fingerprint profiles were seen in CD−/− neurons but not in CB−/−CL−/− neurons (Figure 3F). In CD+/− or CB+/−CL+/− mouse neurons, typical dense bodies were detected (Figure 3C), while autophagosome-like structures were only occasionally seen. In these control mouse neurons, however, GROD-like inclusions were totally absent (Supplemental Figure 3 at http://ajp.amjpathol.org). These results suggest that the common neuropathological findings of these two mutant mice are the accumulation of GROD-like inclusions and autophagosome-like structures in neuronal perikarya. Neuropathological findings of CD−/− and CB−/−CL−/− mouse brains are summarized in Table 1.

The Volume Density of Autophagosome-Like Inclusion Bodies Increases with Age in CD−/− and CB−/−CL−/− Mouse Neuronal Perikarya

To understand characteristics of inclusions in CD−/− and CB−/−CL−/− mouse neurons, the volume density (percent volume) of various lysosomal structures in the neuronal perikarya was analyzed using the point counting method. According to the morphological criteria as shown in Figure 3G, the volume densities of AVi, AVd, GROD-like inclusions, fingerprint profiles, and dense bodies were determined. In CD+/− neurons, the volume density of dense bodies gradually increased and became 2.5 ± 0.48% (mean ± SE) at P23 (Figure 3G). Although autophagosomes were also detected in these control neurons, the volume densities of AVi and AVd were very low and 0.39 ± 0.19% and 0.37 ± 0.16% at P23, respectively (Figure 3G). In CD−/− neurons, dense bodies were hardly seen from P8 to P23, while, as stated above, GROD-like inclusions was abundant and its density changed from 4.9 ± 0.62% at P8 to 20.5 ± 1.63% at P23 (Figure 3G). As for AVi and AVd, their volume densities increased rapidly from P15 to P23; in particular, the volume density of AVd at P23 was 5.94 times larger than
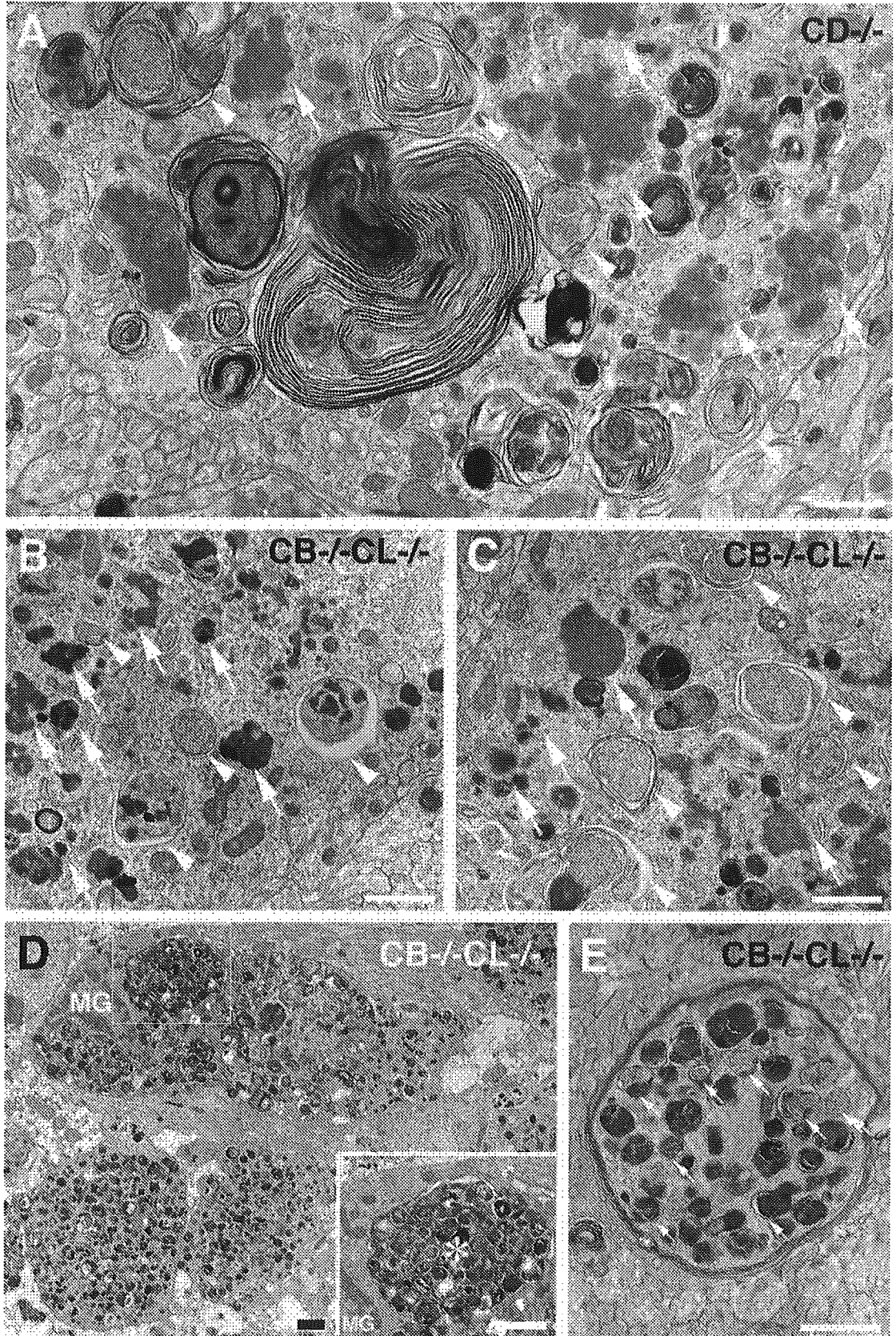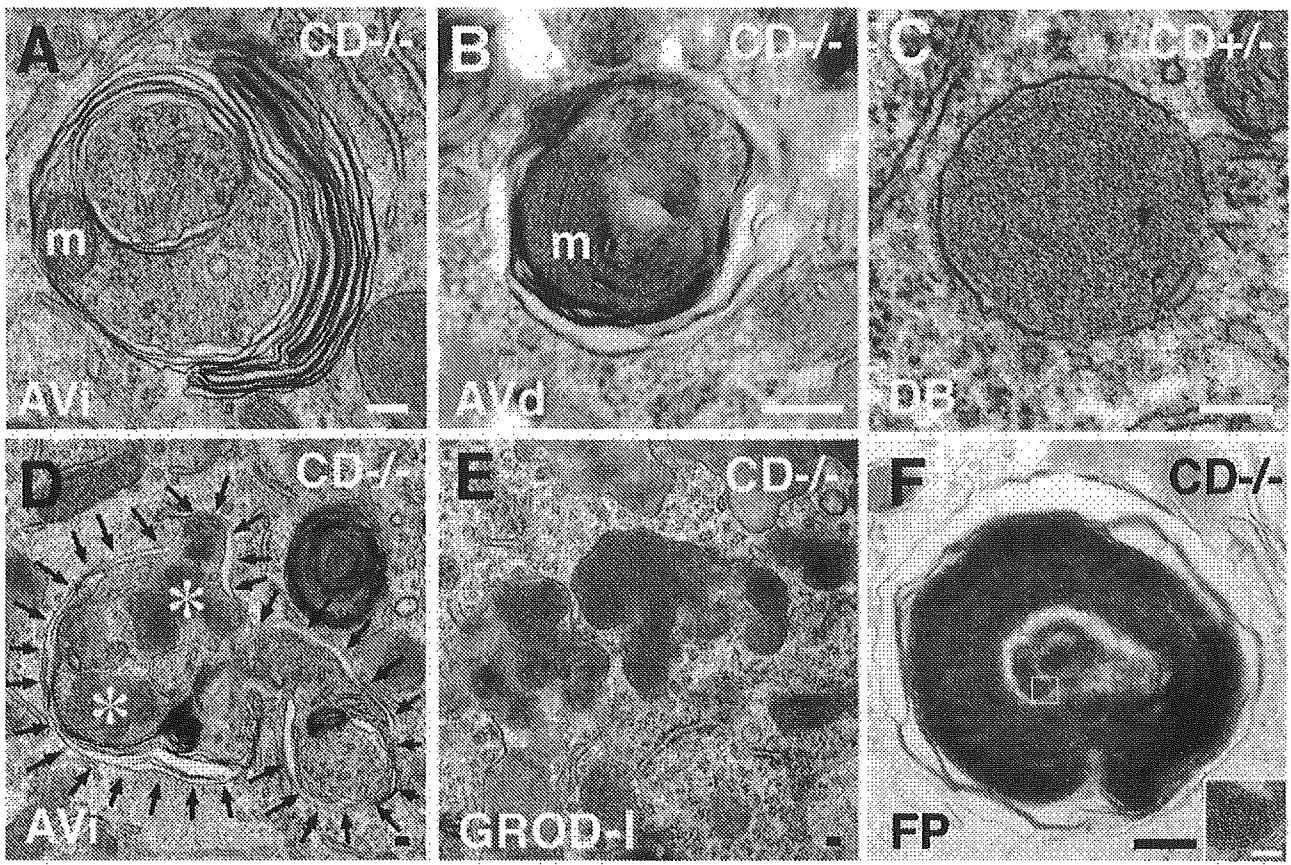
Figure 3. Morphometric analysis of various lysosomal compartments in the perikarya of CD−/− and CD+/− mouse neurons. A–E: Representative examples of early (AVi; A, D) and late (AVd; B) AVs, granular osmiophilic deposit-like inclusions (GROD-l; E), and a fingerprint profile (FP; F) from CD−/− neurons obtained at P23, and a normal dense body (C) from a CD+/− neuron obtained at P23 are shown. In AVi, a mitochondrion (m) together with part of the cytoplasm is clearly visible (A), while in AVd, a mitochondrion with partially degraded cytoplasmic materials is also identifiable. D: AVi that contains GROD-l is detectable. Small arrows show double membranes surrounding GROD-l (asterisks). To show the fingerprint pattern clearly, a boxed area in F is enlarged in an inset. G: The volume densities (%) of AVi, AVd, dense body, GROD-l, and fingerprint profiles (FPs) in the perikarya of neurons in the layer V of the cerebral cortex obtained from CD+/− and CD−/− mice at P8, P15, and P23 and CB−/−CL−/− and CB+/−CL+/− littermates at P13 are shown as a stack bar chart. Scale bars: 0.1 μm (A–F); 0.2 μm (inset in F).

that at P15 and was 4.48 ± 0.7%, while that of AVi at P23 was 3.6 times higher than that at P15 and was 10.1 ± 1.31% (Figure 3G). As shown in Figure 2D, GROD-like inclusions was often enwrapped by double-membrane saccules together with part of the cytoplasm and half of AVi contained GROD-like inclusions at P23, while 20% of GROD-like inclusions was found in AVi. In addition to

GROD-like inclusions, fingerprint profiles that were also characteristic ultrastructures in NCLs, showed their volume density as 6.7 ± 0.97% at P23 (Figure 3, F and G). Moreover, the volume density of total lysosomal structures at P23 was 3.3% in control mouse neurons, whereas it reached nearly 42% in CD−/− neurons. These data suggest that abundant autophagosome formation in

Figure 2. Electron micrographs of neuronal cells from brains of a CD−/− mouse at P23 (A) and a CB−/−CL−/− mouse at P12 (B–E). A–C: In the perikarya of cerebellar Purkinje cells (A, C) and a cerebral cortical neuron (B), numerous dense bodies, which resemble granular osmiophilic deposit-like inclusions (GROD-l) (arrows), can be seen, and vacuolar/autophagosome-like structures (arrowheads) encircled by ER-like membrane saccules and containing cytoplasmic organelles together with part of the cytoplasm are clearly visible. These autophagosome-like structures and GROD-like inclusions are often encircled by ER-like membrane saccules or multilamellated structures. D and E: In axons located in the corpus callosum of the same mouse as in B and C, accumulated autophagosome-like structures can be seen (D), while these structures accumulated in a myelinated axon are distinctly encircled by ER-like membrane saccules (E, small arrows). Moreover, a microglia-like cell (MG) appears in this field and possesses electron-dense heterophagosomes (asterisk) containing degenerating axons with numerous autophagosome-like structures (inset in D). The cytoplasm around the heterophagosome in the cell appears intact. Scale bars, 1 μm.

Table 1.   Pathological Findings Observed in CD−/− and CB−/−CL−/− Mice

	CD−/− mice	CB−/−CL−/− mice
Duration of life	Around P26	Around P14
Tremor	Positive	Positive
Onset of the tremor	Around P20	Around P10
Autofluorescence in neurons	Fine granular at P13 and massive at P23	Fine granular at P13
Autofluorescence in microglial cells	Massive	Massive
PAS	Positive	Positive
Accumulation of subunit c in neurons	Fine granular at P13 and massive at P23	Fine granular at P13
Accumulation of subunit c in microglial cells	Massive	Massive
AVs in the perikarya and dendrites of neurons	Positive	Positive
Multilayered AVs	Frequent	Occasional
GROD-like inclusions	Positive	Positive
GROD-like inclusions within AVs	Positive	Positive
Fingerprint profiles	Positive	Negative
Curvilinear profiles	Negative	Negative

PAS, periodic acid-Schiff staining; AV, autophagic vacuole; GROD, granular osmiophilic profiles.

CD−/− mouse neurons from P15 to P23 contributes to the accumulation of lysosomal structures.

In CB+/−CL+/− neurons, the volume density of dense bodies was 1.8 ± 0.18% (mean ± SE) at P13, while that of AVd was very low (0.32 ± 0.18%) (Figure 3G). In CB−/−CL−/− neurons, dense bodies were hardly seen at P13, while the volume densities of AVi and AVd were 4.91 ± 3.61% and 1.14 ± 1.28%, respectively (Figure 3G). As stated above, GROD-like inclusions were abundant and its density reached 24.1 ± 0.53% at P13; this value corresponded well with that in CD−/− neurons at P23 (Figure 3G). Like CD−/− neurons, GROD-like inclusions in CB−/−CL−/− neurons were often enwrapped by double-membrane saccules together with part of the cytoplasm and ~75% of AVi contained GROD-like inclusions at P13, while 15% of GROD-like inclusions were found in AVi. The volume density of total lysosomal structures at P13 was 2.1% in control mouse neurons, whereas it reached nearly 30% in CB−/−CL−/− neurons. These data suggest that like CD−/− neurons, the contribution of abundant autophagosome formation to the accumulation of lysosomal structures is also evident in CB−/−CL−/− mouse neurons.

The Level of Autophagosome-Associated LC3-II Increases in CD−/− and CB−/−CL−/− Mouse Brains

LC3-I, a cytosolic form, is known to be converted to LC3-II, a membrane-bound form when autophagy is induced.[14] Because numerous autophagosome-like structures were detected in the perikarya of mutant mouse brains, we examined the molecular forms of LC3 in the tissues by Western blotting. As shown in Figure 4, A and B, LC3-I predominated in control brains obtained at any of the stages examined, whereas the LC3-II form gradually increased in CD−/− mouse brains in an age-dependent manner. In fact, the ratios of the amounts of LC3-II to LC3-I were significantly higher in the CD−/− mouse brains than in the control brains after P8 (Figure 4B). An increase in the amount of the LC3-II form was also found in CD−/− retina at P24 when massive retinal degenera-

tion occurred (Figure 4, C and D).[21] We also examined changes in the molecular forms of LC3 in CB+/−CL+/− and CB−/−CL−/− mouse brains at P13. Like CD−/− mouse brains, the LC3-II form predominated only in brain extracts obtained from CB−/−CL−/− mice (Figure 4, E and F).

Because molecular forms of LC3 in CD−/− mouse brains changed drastically from P8 to P23 and differed from those in CD+/− mouse brains at each stage, expression of LC3 mRNA in these mouse brains were also examined by RT-PCR. As shown in Figure 4G, no clear-cut changes in expression levels of LC3 mRNA were detected between CD−/− and CD+/− mouse brains at each stage and in CD−/− mouse brains between stages. Expression levels of LC3 mRNA were also analyzed between CB−/−CL−/− and CB+/−CL+/− mouse brains at P13, but no difference was discerned between them (Figure 4H). These results indicate that the cytosolic form of LC3 is predominant in intact brains at any of the stages examined, while the membrane-bound form of LC3 became a major form in both CD−/− and CB−/−CL−/− brains at their terminal stages, respectively.

Immunolocalization of LC3 in CD−/− and CB−/−CL−/− Mouse Brains

Because autophagosome-like structures were abundant in mutant neurons and the membrane-bound form of LC3 became predominant in these mouse brains, we examined the localization of LC3 in control and mutant mouse brains using an anti-LC3 antibody. In control mouse brains, diffuse and/or fibrillary staining of LC3 was detectable in the dendrites and perikarya of cerebral cortical neurons (Figure 5A, inset), as has been described previously for rat cerebellum.[37] In dendrites of CD−/− neurons at P23, the staining patterns were similar to those of the control neurons, whereas intense granular staining of LC3 was detected in the perikarya of neurons in the cerebral cortex of CD−/− mice (Figure 5B, inset).

In CB−/−CL−/− mice, immunopositive granules for LC3 were abundantly demonstrated in the perikarya of Purkinje cells in the cerebellum (Figure 5D, inset) and
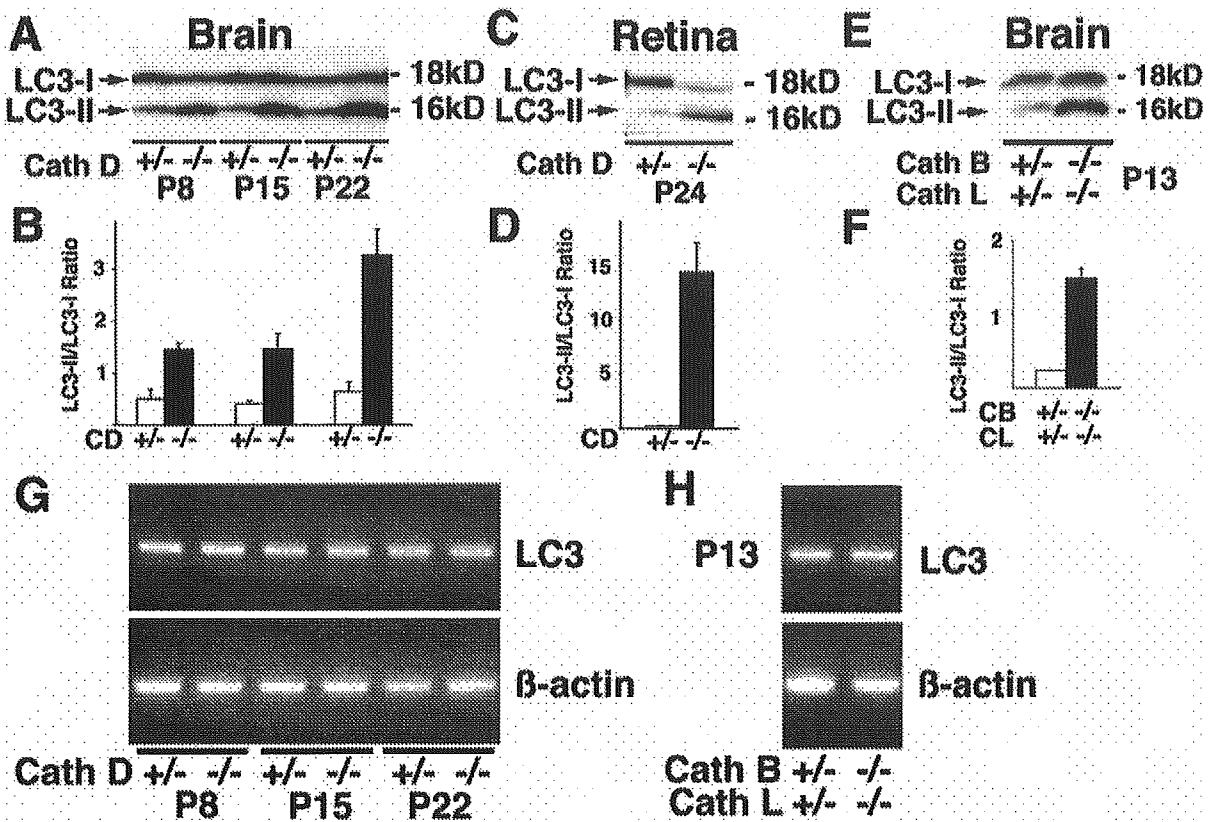
Figure 4. Molecular forms of LC3 in nervous tissues of CD−/− and CB−/−CL−/− mice and their littermate controls. **A** and **B:** Immunoblotting of LC3 in brains of CD−/− mice and their littermate controls (CD+/−) obtained at P8, P15, and P22 (**A**), and ratios of densities of LC3-II to LC3-I protein bands (**B**). **C** and **D:** Immunoblotting of LC3 in retinae of CD−/− mice and their littermate controls (CD+/−) obtained at P24 (**C**), and ratios of densities of LC3-II to LC3-I protein bands (**D**). **E** and **F:** Immunoblotting of LC3 in brains from CB−/−CL−/− and CB+/−CL+/− mice at P13 (**E**), and the ratios of densities of LC3-II to LC3-I protein bands (**F**). **G** and **H:** Expression of LC-3 mRNA in brain tissues of CD−/− and CB−/−CL−/− mice and their littermate controls. A RT-PCR study. Expression levels of LC-3 mRNA do not differ between CD−/− and CD+/− mice at all stages examined (**G, top**), and between CB−/−CL−/− and CB+/−CL+/− mice (**H, top**). **Bottom** panels show β-actin mRNA, used as internal controls.

cerebral cortical neurons (data not shown), whereas diffuse and fibrillary staining was distinct in the perikarya and dendrites of Purkinje cells (Figure 5C, inset) and cerebral cortical neurons of CB+/−CL+/− mice. Because autophagosome-like vacuoles were abundantly shown in axons in the corpus callosum of CB−/−CL−/− mouse brains (Figure 2, D and E), immunostaining for LC3 was applied to the region; numerous LC3-positive granules were demonstrated in the CB−/−CL−/− axons (Figure 5F), but no positive staining of LC3 was detected in the axons of the control corpus callosum (Figure 5E).

We further examined whether these LC3-positive granules in the neuronal perikarya of CB−/−CL−/− neurons also possess lysosomal characteristics by double-immunofluorescent staining for LC3 and lamp1, an abundant lysosomal integral membrane protein. Even in the CD−/− mouse brains at P23, it was possible to find cerebral cortical regions that did not emit autofluorescence. As shown in Figure 6, A–F, some LC3-positive granules were also stained for lamp1 in the cytoplasm of cerebral cortical neurons and cerebellar Purkinje cells in CD−/− and CB−/−CL−/− mice, but a considerable number of LC3-positive granules, which were relatively large in size and intensity, were distinct from lamp1-positive granules, indicating that these granules were nascent, because they are free from any lysosomal characteristics. These results suggest that

the number of LC-3-immunopositive autophagosomes/autophagolysosomes is increased in neuronal cells of CD−/− and CB−/−CL−/− mouse brains.

In addition to the neuronal perikarya, the accumulation of autophagosome-like structures was shown in myelinated and unmyelinated axons and microglia-like cells in the corpus callosum of the mouse brain (Figure 2, D and E), double-immunofluorescent staining for LC3 and lamp1 or F4/80 was performed in the region. Most LC3-positive structures were negative for lamp1 in the corpus callosum (Figure 6, G–I), whereas F4/80-positive microglial cells occasionally enwrapped LC3-positive granules (Figure 6, J–L). These data suggest that accumulated vacuolar structures in axons of the corpus callosum of the mutant mouse brains are nascent autophagosomes and microglial cells invaded into the region possess heterophagosomes containing autophagosomes.

LC3 Is Localized on the Isolation Membrane of Autophagosomes in Neurons of CD−/− and CB−/−CL−/− Mouse Brains

Because LC3-immunopositive granules were abundant in neurons of mutant mouse brains, we further examined the precise localization of LC3 by immunoelectron micros-
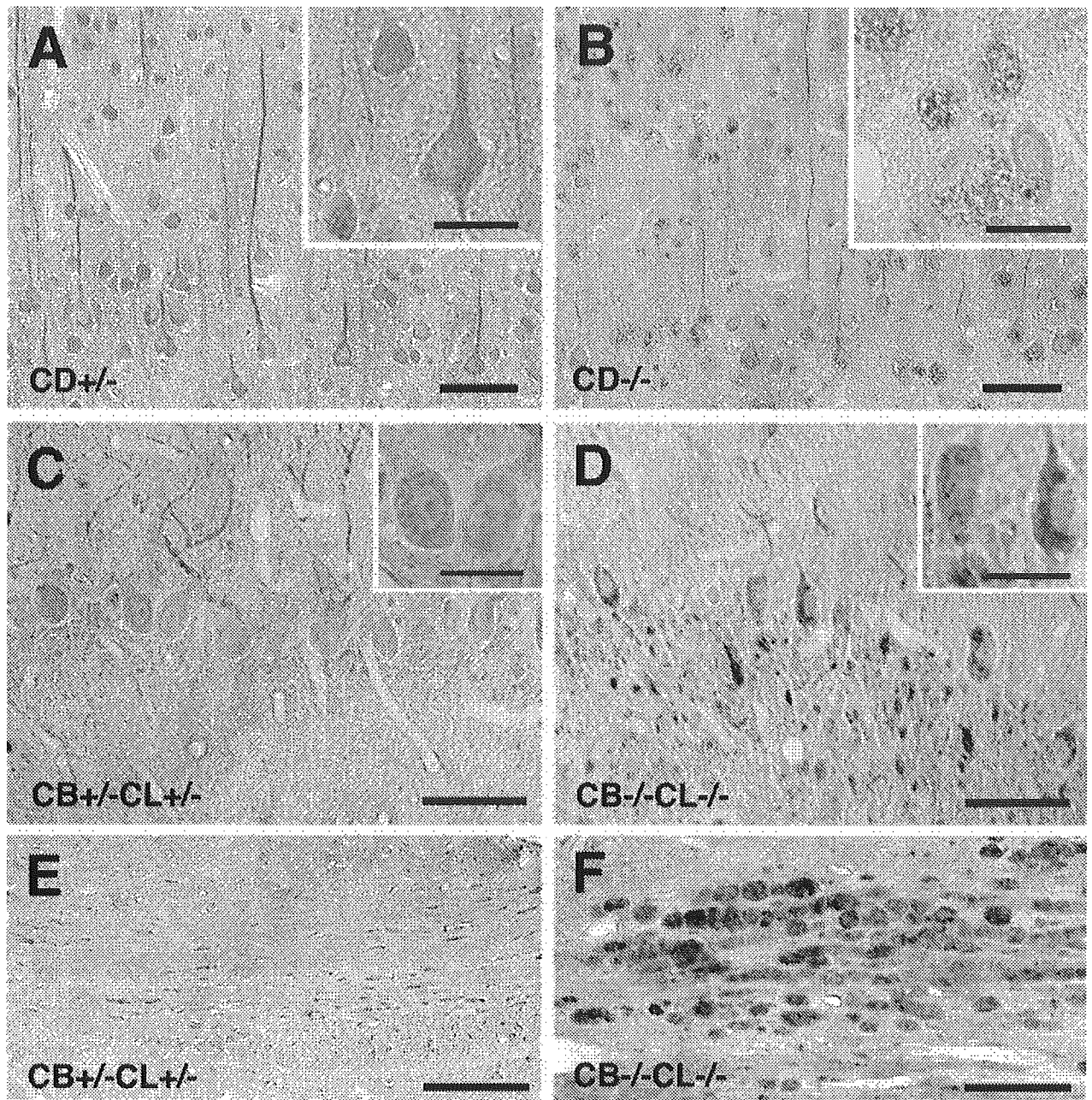
Figure 5. Immunohistochemical staining of LC3 in brain tissues of CD−/− and CB−/−CL−/− mice and their littermate controls. **A** and **B:** Cerebral cortical regions of CD+/− (**A**) and CD−/− (**B**) mouse brains at P24. Positive staining of LC3 appears fibrillary in dendrites of pyramidal neurons and diffuse in their perikarya (**A, inset**). Its staining is also fibrillary in dendrites of the neurons but appears granular in their perikarya (**B, inset**). **C** and **D:** Purkinje cells in the cerebellum of CB+/−CL+/− (**C**) and CB−/−CL−/− (**D**) mice at P12. Fibrillary staining of LC3 is demonstrated in dendrites of Purkinje cells from both control and mutant mice (**C, D**), whereas its staining is relatively weak and diffuse in the perikarya of CB+/−CL+/− control neurons (**C, inset**) but intense and granular in those of CB−/−CL−/− neurons (**D, inset**). **E** and **F:** Nerve fibers in the corpus callosum of CB+/−CL+/− (**E**) and CB−/−CL−/− (**F**) mice at P12. No clear-cut staining for LC3 can be seen in the control axons (**E**), whereas intensely stained dots are accumulated in the mutant axons. Scale bars: 50 μm (**A–F**); 20 μm (**insets in A–D**).

copy. We first attempted to use immunoelectron micros-copy using postembedding and cryothin section immu-nogold methods, but were not able to realize positive signals. We therefore used the SDS-FRL method that was originally developed to study the two-dimensional distri-bution of integral membrane proteins and phospholipids in biomembranes, using weakly fixed materials.[25] As shown in Figure 7, A–C, specific gold particles indicative of LC3 were clearly demonstrated on the membranes of

perikaryal granules in anterior spinal neurons and cere-bellar Purkinje cells of CD−/− mice. The membranes of the granules that were labeled with gold particles for LC3 possessed almost no intermembrane particles (Figure 7A). In some cases, granular structures with membranes labeled by the gold particles were further enwrapped by membrane structures (Figure 7B), while positive deposits were found on membranes of multilamellar bodies (Fig-ure 7C). Considering the fact that granules with negligible
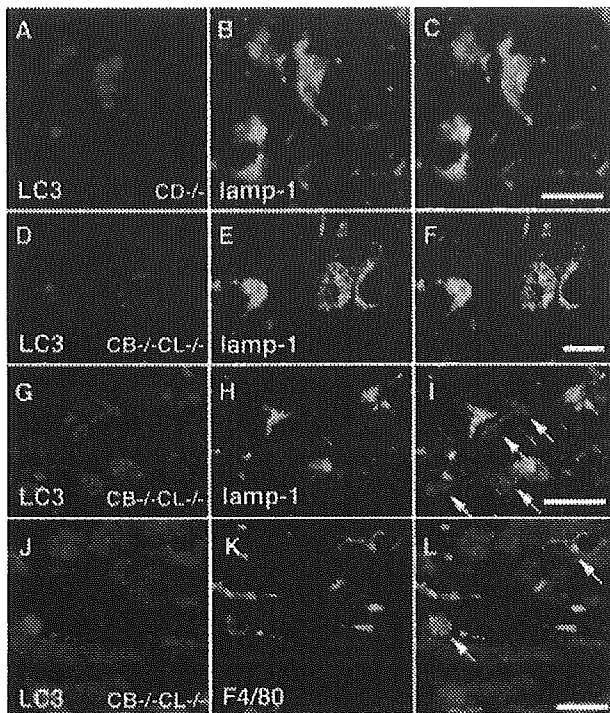
Figure 6. Double-immunofluorescent staining of LC3 (**A, D, G, J**; red color) with lamp1 (**B, E, H**; green color) in cerebral cortical neurons (**A–C**) of CD−/− mice at P23, cerebellar Purkinje cells (**D–F**), and the corpus callosum (**G–I**) of the CB−/−CL−/− mice at P13 or with F4/80 (**J**, green color) in the corpus callosum (**J–L**) of the CB−/−CL−/− mice at P13. **A–F:** A considerable number of LC3-positive granules are also stained for lamp1, but certain numbers of LC3-positive granules (**arrows**), which are large in size and stain intensely, are distinct from lamp1 (**C** and **F**, overlay). **G–I:** LC3-positive staining in the corpus callosum (**arrows**) is primarily distinct from lamp1 staining (**I**, overlay). **J–L:** F4/80-positive microglial cells possess LC3-positive staining (**arrows**) (**L**, overlay). Scale bars, 15 μm.

Figure 7. Immunocytochemical freeze-fracture replica images of an anterior spinal neuron (**A**) and cerebellar Purkinje cells (**B, C**) of CD−/− mice at P20 incubated with an anti-LC3 antibody. **A:** Immunogold labeling is observed on the membrane-bound organelles accumulated in the cytoplasm of the anterior neuron (**arrowheads**). **B** and **C:** In the perikarya of Purkinje cells, positive signals are well localized on membranes of two granules that are further encircled by membrane structures (**thin arrows**) (**B**), while they are also detected on multilamellar membranes (**thick arrows**). Scale bars, 0.25 μm.

numbers of intermembrane particles and multilayered vacuoles are typical of autophagosomes when observed by freeze-fracture electron microscopy, these data suggest that LC3, probably the LC3-II form, is specifically localized on the isolation membrane of autophagosomes in mutant mouse neurons.

GFP-LC3 Is Converted into LC3-II and Labels Accumulated Autophagosomes in GFP-LC3/ CD−/− Mouse Brains

Using GFP-LC3 transgenic mice,[23] we generated CD−/− mice expressing GFP-LC3 to further confirm the accumulation of autophagosomes in neurons of CD−/− mouse brains. Like in CD+/− and CD−/− mouse brains, the LC3-I form was a major form in GFP-LC3/CD+/+ mouse brains, while the LC3-II form became increased in GFP-LC3/CD−/− mouse brains (Figure 8A). The ratios of protein amounts of LC3-II to LC3-I were examined, and found to be similar between CD+/− and GFP-LC3/ CD+/+ mouse brains or CD−/− and GFP-LC3/CD−/− mouse brains. In the case of GFP-LC3, the amount of GFP-LC3-I was much larger than that of GFP-LC3-II in both GFP-LC3/CD+/+ and GFP-LC3/CD−/− mouse brains. However, GFP-LC3-II distinctly appeared in GFP-

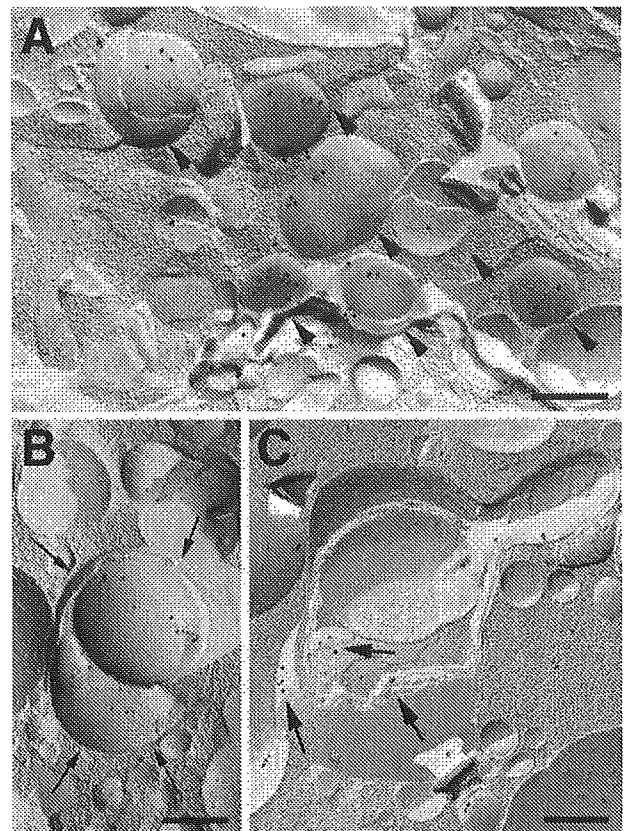LC3/CD−/− brains, but only faintly in GFP-LC3/CD+/+ brains (Figure 8A).

When immunostained with either anti-LC3 or anti-GFP, intense fibrillary staining was detected in dendrites of cerebellar Purkinje cells in both GFP-LC3/CD+/+ and GFP-LC3/CD−/− mice (Figure 8, B–E), while granular staining appeared in the perinuclear region of the cells in GFP-LC3/CD−/− mice (Figure 8, C and E). The positive staining in both GFP-LC3/CD+/+ and GFP-LC3/CD−/− mouse brains, however, was much more intense when stained with anti-LC3 than that when stained with anti-GFP (Figure 8, B–E), because anti-LC3 recognizes both endogenous LC-3 and GFP-LC3. In some cases, granular immunodeposits for LC3/GFP-LC3 were detected in dendrites of GFP-LC3/CD−/− Purkinje cells (Figure 8, C and E). To confirm the relationship between lysosomes and autophagosomes, GFP-LC3/CD−/− mouse cortical neurons were stained for lamp1, and found that lamp1 immunoreactivity was often localized in GFP-LC3-positive granules, but a considerable number of GFP-LC3-positive granules were free from lamp1 immunoreactivity (Figure 8, F–H). These data confirmed the enormous accumulation of autophagosomes in neurons of CD−/− mouse brains.
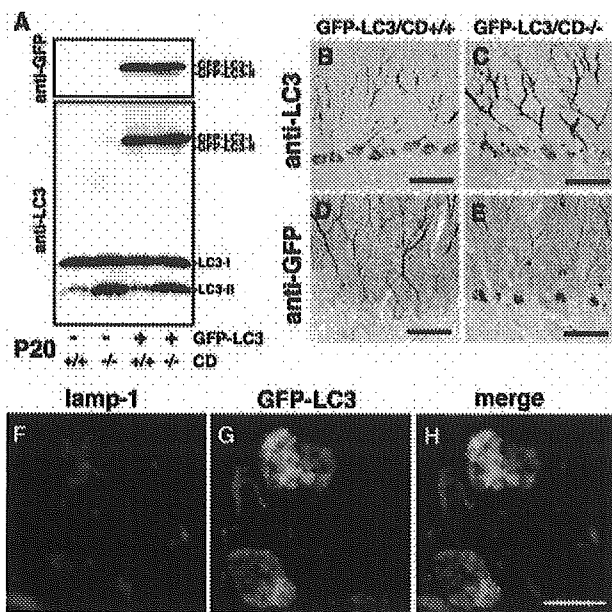
Figure 8. Expression of GFP-LC3 in brains of GFP-LC3/CD−/− mice. **A:** Molecular forms of GFP-LC3 in brains of GFP-LC3/CD+/+ and GFP-LC3/CD−/− mice at P20. GFP-LC3-I is a major form in both GFP-LC3/CD+/+ and GFP-LC3/CD−/− brains, whereas GFP-LC3-II appears faintly in GFP-LC3/CD+/+ brains and distinctly in GFP-LC3/CD−/− brains when immunostained with either anti-GFP or anti-LC3. Moreover, the quantitative relationship of LC3-II to LC3-I in brains of CD+/+ and CD−/− mice does not differ depending on GFP-LC3 expression. **B–E:** Immunohistochemical images of GFP-LC3 and LC3 (**B** and **C**), or GFP-LC3 (**D** and **E**) in cerebellar Purkinje cells of GFP-LC3/CD+/+ (**B** and **D**) and GFP-LC3/CD−/− (**C** and **E**) mice at P20. Immunoreactivity for LC3-GFP and LC3, that was immunoreacted with anti-LC3, is more distinct and intense in dendrites and bodies of Purkinje cells than that for GFP-LC3 that was immunostained with anti-GFP. Diffuse or fibrillary staining for GFP-LC3 and LC3, or GFP-LC3 is clear in dendrites and bodies of Purkinje cells from a GFP-LC3/CD+/+ mouse, whereas granular staining for them (spheroids, **arrows**) is observed not only in Purkinje cell bodies but also in their dendrites from a GFP-LC3/CD−/− mouse. **F–H:** Double-fluorescence images of lamp1 (red color, **F**) and GFP-LC3 (green, **G**) in cerebral cortical neurons of GFP-LC3/CD−/− brains at P20. Lamp1 immunoreactivity is often localized in GFP-LC3-positive granules, but a considerable number of GFP-LC3-positive granules are distinct from lamp1 immunoreactivity (**H**). Scale bars: 50 μm (A–E); 10 μm (F–H).

Figure 9. Expression of LC3 in peripheral tissues of CD−/− (A–E) and CB−/−CL−/− (F, G) mice and their littermate controls (CD+/−, CB+/−CL+/−). A and B: Molecular forms of LC3 in the liver of CD+/− and CD−/− mice at P15 and P22 (A), and densities of LC3-II (B). C and D: Molecular forms of LC3 in the heart of CD+/− and CD−/− mice at P15 and P22 (C), and densities of LC3-II (D). E and F: Molecular forms of LC3 in the liver and heart of CB+/−CL+/− and CB−/−CL−/− mice at P13 (E), and densities of LC3-II (F).

LC3 in Peripheral Tissues of CD−/− and CB−/−CL−/− Mice

The accumulation of lysosome-like structures immunopositive for subunit c has been previously shown in peripheral tissue cells of CD−/− mice, including hepatocytes and cardiac muscles.[11] We therefore examined the protein amounts of LC3-I and LC3-II in the liver and heart of both CD+/− and −/− mice, and the localization of LC3 in these tissue cells.

Different from brain tissues, LC3-I was only weakly detected in hepatic (Figure 9, A and B) and cardiac (Figure 8, C and D) tissues from CD+/− mice, and almost absent in those from CD−/− mice. On the contrary, the amounts of LC3-II were high in hepatic (Figure 9, A and B) and cardiac (Figure 9, C and D) tissues of CD−/− mice even at P15, compared to those of CD+/− mice, respectively. The LC3-II form was even more elevated in the CD−/− tissues at P22 than in the CD+/− tissues. Immunohistochemical observations showed that granular staining of LC3 was distinctly detected in hepatocytes
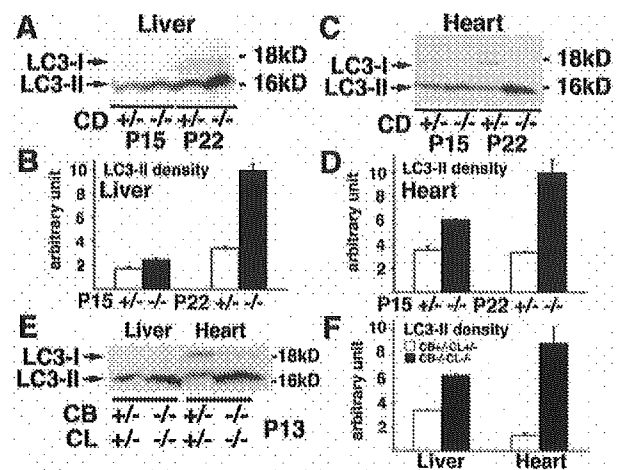
and cardiac muscle cells of CD−/− mice, but not in those of CD+/− mice (Figure 10, A–D).

In addition to peripheral tissues from CD−/− mice, the molecular forms of LC3 were also examined in cardiac and hepatic tissues from CB−/−CL−/− and CB+/−CL+/− mice at P13. Like CD−/− mouse tissues, the amounts of LC3-II were significantly high in both cardiac and hepatic tissues from the CB−/−CL−/− mice, compared to those from CB+/−CL+/− mice (Figure 9, E and F).

Discussion

The main findings of the present study using electron microscopic, laser scanning microscopic, and biochem-
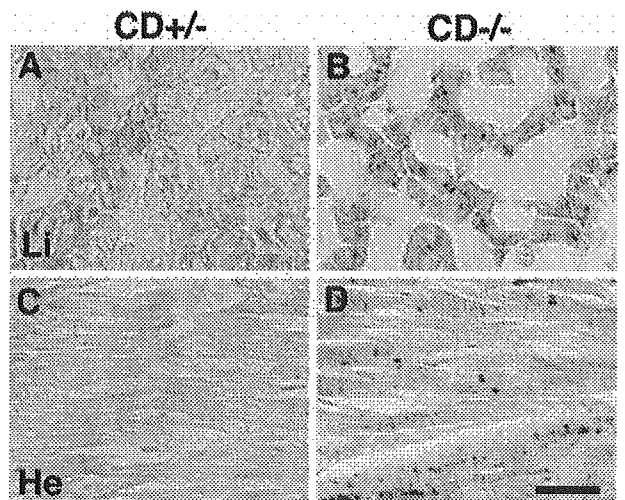

Figure 10. Immunostaining of LC3 in hepatic (A, B) and cardiac (C, D) tissues of CD+/− (A, C) and CD−/− (B, D) mice at P23. Punctate staining for LC3 is distinct in hepatocytes and cardiac muscular cells of CD−/− mice. Scale bar, 20 μm.